A METHOD TO DRAMATICALLY DECREASE THE REQUIRED DEPLETION POWER OF STED SUPER-RESOLUTION MICROSCOPY AND HIGH POWER OPERATION OF NSOM PROBES

A Dissertation

by

DANIEL MCBRIDE

Submitted to the Office of Graduate and Professional Studies of
Texas A&M University
in partial fulfillment of the requirements for the degree of

DOCTOR OF PHILOSOPHY

Chair of Committee,	Chin Su
Committee Members,	Jun Kameoka
	Alvin Yeh
	Arum Han
Head of Department,	Miroslav Begovic

May 2017

Major Subject: Electrical Engineering

ABSTRACT

A versatile STED microscope using a supercontinuum light source for selecting various excitation and depletion wavelengths needed for different fluorescent dyes was designed and built. Using a 0.9 NA microscope objective and 100 nm diameter beads, 90 nm de-convoluted lateral super-resolution was achieved.

A major drawback of traditional STED microscopy is the high depletion power required, which alters sample integrity and causes dye bleaching. A new version that should dramatically decrease the required depletion power is proposed and built. This version uses a common vortex phase plate for both the excitation and depletion beams which also improves mechanical stability of the overlapping focal spots. Rigorous electromagnetic and rate equation analysis shows that the required depletion optical power is decreased by a factor of about six in comparison with traditional method for achieving the same lateral super-resolution.

In a separate project, in order to introduce more optical power into a NSOM probe without damaging the probe, epoxy heat sinks were fabricated on the probe tip. Optical imaging and optical power measurements were used to verify that the NSOM probe was not damaged when 405 nm light, at an input power of 21.4 mW, was coupled into the NSOM probe. The NSOM probe was used to ex-pose though 93 nm thick photoresist. The maximum scan rate was approximately 300 μm/sec with a 100 nm aperture NSOM probe.

DEDICATION

This thesis is dedicated to my parents.

ACKNOWLEDGEMENTS

I would like to thank my committee chair, Dr. Chin Su, for his guidance and support during my research. I would also like to thank my committee members, Dr. Jun Kameoka, Dr. Arum Han, and Dr. Alvin Yeh for their guidance and helpful discussions.

Thanks also go to my friends and colleagues.

I would like to acknowledge the facilities at Texas A&M University, especially the Material Characterization Facility and Center for Nanoscale Science & Technology.

Finally, thanks to my parents and brother for their encouragement.

CONTRIBUTORS AND FUNDING SOURCES

This work was supervised by a dissertation committee consisting of Professors Chin Su, Jun Kameoka, and Arum Han of the Department of Electrical Engineering and Professor Alvin Yeh of the Department of Biomedical Engineering.

All work for the dissertation was completed by the student, under the advisement of Professor Chin Su of the Department of Electrical Engineering.

There are no outside funding contributions to acknowledge related to the research and compilation of this document.

NOMENCLATURE

BS	Beam Splitter
BSE	Backscattered Electrons
CCD	Charge-coupled Device
EDS	Energy-dispersive X-ray Spectroscopy
NA	Numerical Aperture
NSOL	Near-field Scanning Optical Lithography
NSOM	Near-field Scanning Optical Microscopy
PBS	Polarized Beam Splitter
PMT	Photo Multiplier Tube
QWP	Quarter Wave Plate
RIE	Reactive Ion Etching
SEM	Secondary Electron Microscopy
STED	Stimulated Emission Depletion
VPP	Vortex Phase Plate

TABLE OF CONTENTS

LIST OF FIGURES

Page

LIST OF TABLES

Page

1. INTRODUCTION

Near-field scanning optical microscopy

Studying samples under high magnification is important in many areas such as engineering and material science. The spatial resolution attainable with optical microscopes is limited to about half the wavelength of the light source if a high numerical aperture microscope objective is used. One approach to overcome the diffraction limit is by using Near Field Scanning Optical Microscopy (NSOM) [1]. NSOM breaks the diffraction limit by exploiting evanescent waves. Evanescent waves are collected in the near field by placing the detector very close to the specimen surface. This allows the surface to be inspected with high spatial resolution. Using NSOM, the resolution of the image is limited by the size of the detector's aperture, not the wavelength of the illuminating light [2].

NSOM uses evanescent fields which only exist very close to the surface of the specimen. Evanescent fields carry high frequency spatial information, but the intensity of the evanescent field decays exponentially with distance from the specimen. So, the detector must very close to the sample, and the illuminating power of the light source must overcome the background noise. Therefore, NSOM is primarily a surface inspection technique. To form an image, the detector is raster scanned across the sample using piezo stage. A feedback system is used to maintain separation between the detector and the specimen [3].

Practical NSOM systems employ a fiber probe which is coated with a thin layer of metal [4]. The intensity of the evanescent field outside the probe's metal aperture decays

exponentially. Compared to far-field microscopy, NSOM probes do not have high light intensity emitting from the probe. The light transport efficiency of NSOM probes is <0.01%, and most of the laser energy is dissipated into heat around the NSOM probe aperture. Using higher laser power increases the temperature of the NSOM probe. The consequent damage of the NSOM probe can cause malfunction of the NSOM system [5-8]. To avoid damage to the NSOM probe, the laser power must be reduced, causing image acquisition times to be very long.

Stimulated emission-depletion microscopy

Fluorescence microscopy is a type of optical microscopy which use visible light, fluorescent probes, and lenses to examine structures within a cell. Fluorescence microscopes rely on the principles of fluorescence and phosphorescence to study cellular features [9]. Fluorescence microscopy uses a narrow set of wavelengths of light to illuminate the sample. These wavelengths of light interact with the fluorescent probes in the sample. The fluorescent probes emit longer wavelengths of light, and this emitted light comprises the image.

Due to the diffraction of light, the maximum spatial resolution achievable using fluorescence microscopy is limited to approximately half the wavelength of light if a high numerical aperture (NA) lens is used. Stimulated emission-depletion (STED) microscopy is one technique which can achieve resolution beyond the diffraction limit. STED creates super-resolution images by deactivation of fluorophores, reducing the area of illumination at the focal point [10]. Stefan Hell and Jan Wichmann first described the technique in 1994 [11]. The technique was demonstrated experimentally in 1999 [12]. STED microscopy is

a deterministic technique which exploits the non-linear response of fluorophores in order to improve the resolution. Stochastic functional techniques such as stochastic optical reconstruction microscopy and photoactivated localization microscopy use mathematical models to reconstruct an image from a set of diffraction-limited images [13].

Normally, fluorescence occurs by exciting an electron from the ground state into an excited state of a different energy level. When the electron relaxes back from the excited state to the ground state, it emits a photon. STED microscopy interrupts this process by selectively deactivating the fluorescence before the photon is released [14]. The number of incident photons impacts the efficiency of the stimulated emission. If the number of incident photons is large enough, fluorescence would be completely suppressed [15]. This necessitates that the laser must be of high intensity. However, high laser power can cause photo bleaching of the fluorophore.

STED microscopes function by selectively depleting fluorescence in certain regions of the sample while allowing fluorescence from a center focal spot. This focal spot can be engineered using diffractive optical elements [16-18]. Normally, the depletion beam is a torus, and the excitation beam is a conventional Gaussian beam. The depletion beam is generated by circular polarization and a helical phase ramp. Lateral resolution of 2.4 nm was reported using this technique with nitrogen vacancies in a diamond [19], but the achievable lateral resolution is directly proportional to the depletion beam power. Due to photo bleaching of fluorophores, the depletion beam power cannot be arbitrarily increased.

2. FABRICATION OF A NEAR-FIELD PROBE WITH AN EPOXY HEAT SINK*

Overview

The spatial resolution of an optical microscope is limited to approximately half the wavelength of the light source if a high numerical aperture is used. Near-field scanning optical microscopy (NSOM) can overcome the diffraction limit by using a sub-diffraction aperture in close proximity to the sample surface [20]. When light propagates through the NSOM probe, most of the light is absorbed or reflected by the metal coating on the NSOM probe, but a small percentage will propagate through the NSOM aperture as an evanescent wave. According to the Bethe/Bouwkamp model [21], the transmission coefficient scales as approximately D^{-4}, where D is the diameter of the aperture [22, 23]. Higher evanescent wave intensity is desirable, but the intensity of the evanescent field cannot be increased arbitrarily by simply increasing the intensity of the input laser light because the metal coating on the NSOM probe will melt when approximately 2 mW of laser power at a wavelength of 405 nm is coupled into the NSOM probe [24]. Scanning electron microscopy (SEM) images of chemically etched NSOM probes damaged by heating has been reported [25, 26].

Heating of NSOM probes due to high laser power has been studied previously. When laser light is coupled into a NSOM probe, the temperature of the NSOM aperture will increase [27-32]. Temperatures up to 470 °C have been reported [28]. Fluctuations in

* Reprinted with permission from "Near-field scanning optical microscopy probes with heat sinks for higher power operations" by McBride D., Su C. B., 2015, *Mater. Res. Express* (2) 105202, Copyright 2015 by IOP Publishing

the temperature of the NSOM aperture cause fluctuations in the throughput of the NSOM probe due to thermal expansion of the metal coating on the NSOM probe [32]. So, it is desirable to prevent the NSOM aperture from heating during scanning in order to maintain constant NSOM aperture throughput.

The following steps describe the fabrication of NSOM probe with epoxy heat sinks. The epoxy heat sink was fabricated by inserting a standard NSOM probe into a fiber optic ferrule. Epoxy was injected into the ferrule using capillary action. Then, the NSOM aperture was positioned a few microns outside the epoxy surface using an optical microscope. After the epoxy cured, SEM was used to image the NSOM aperture and measure the amount of epoxy on the aperture. Since the extent of the evanescent field from the NSOM aperture is only a few nm, all excess epoxy must be removed from the NSOM aperture. Reactive Ion Etching (RIE) was used to remove the excess epoxy from the NSOM aperture. SEM, Energy-dispersive X-Ray Spectroscopy (EDS), and Backscattered Electrons (BSE) were used to verify the absence of epoxy on the NSOM aperture.

During the RIE step, the presence of the gold coating on the NSOM probe produces the lightning-rod effect due to high electric field intensity around the sharp gold-coated NSOM tip, resulting in anisotropic etching of the epoxy. The etch rate is especially non-uniform within a few microns of the gold coating. The lightning-rod effect can also cause the gold coating on the NSOM probe to be damaged during etching due to ion sputtering. A combination of low power, high pressure, and low temperature were used in order to make the etching more uniform. This etching recipe also favors chemical etching rather than ion sputtering [33], which minimizes ion bombardment of the gold film. Using this

RIE process, the excess epoxy was removed from the NSOM aperture with no observable damage to the gold coating, as verified by SEM, BSE, and EDS.

Process steps for fabrication of NSOM probe with epoxy heat sink

First, the front end of a standard zirconium oxide ferrule was machined using a polycrystalline diamond bit and a lathe so that the ferrule tip diameter was reduced from the standard 2.5 mm to 1 mm. The reduced diameter is favorable for subsequent epoxy injection into the ferrule to form a good epoxy curvature profile. The next step is to guide the NSOM tip from the ferrule back end so that it protrude out from the reduced diameter front end. Note that the ferrule hole diameter is a standard 127 um, thus it is not straightforward to guide the NSOM tip into the ferrule hole as hitting the tip against any part of the ferrule will destroy the tip.

The buffer of a piece of optical fiber was removed, leaving the bare piece of fiber about 10 cm in length. Both ends of the fiber were cleaved and cleaned. With the machined ferrule held in a ferrule holder, the fiber was inserted into the ferrule such that the fiber piece protruded a few microns out of the back end of the ferrule. The NSOM probe and ferrule were translated such that the NSOM tip and the piece of fiber protruding from the back of the ferrule were both observed under the microscope, as shown in Figure 1.

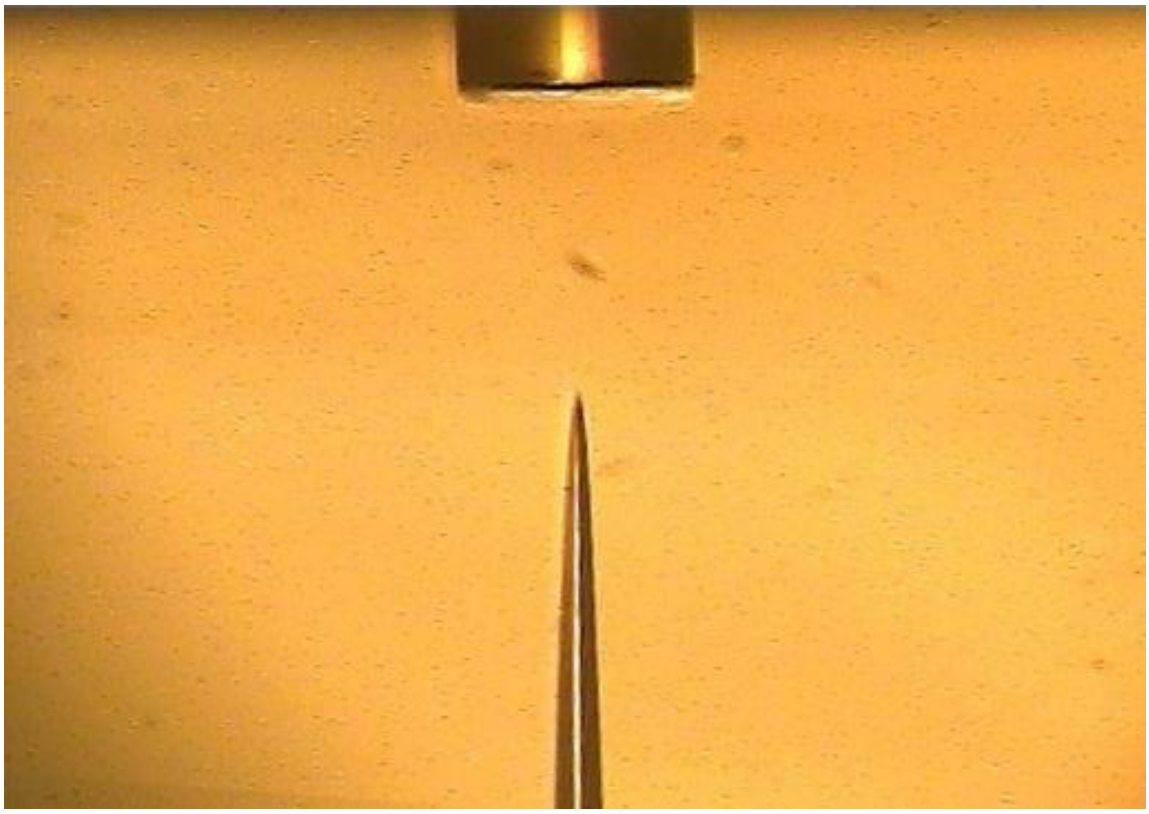

Figure 1. NSOM probe aligned with guiding fiber.

In Figure 1, the bright sharp strip of the fiber's cleave end under the microscope light indicated that the top of the fiber is in focus. Then, the NSOM was also translated so that the tip is also in focus. Then, the NSOM tip was translated down by 127/2 micron and also laterally translated the so it was aimed at the lateral center of the fiber's cleaved end. The NSOM tip was then positioned at the center of the ferrule hole both vertically and laterally. The cleaved fiber was then removed from the ferrule. The NSOM tip was translated into the ferrule hole until the tip protruded out of the machined ferrule's front end by approximately 10-20 µm.

Now, the epoxy injection rod was placed on a micro-translator. Using a syringe, approximately 1 uL of optical epoxy was applied to the tip of the epoxy injection rod. The tip of the epoxy injection rod and the NSOM tip (protruding out of the ferrule) were both positioned within the field of view of the microscope. Then, the epoxy injection rod was translated so that the convex epoxy meniscus at the tip of the rod made physical contact with the front of the machined ferrule. Due to capillary action, epoxy flowed into the front of the ferrule hole (see Figure 2).

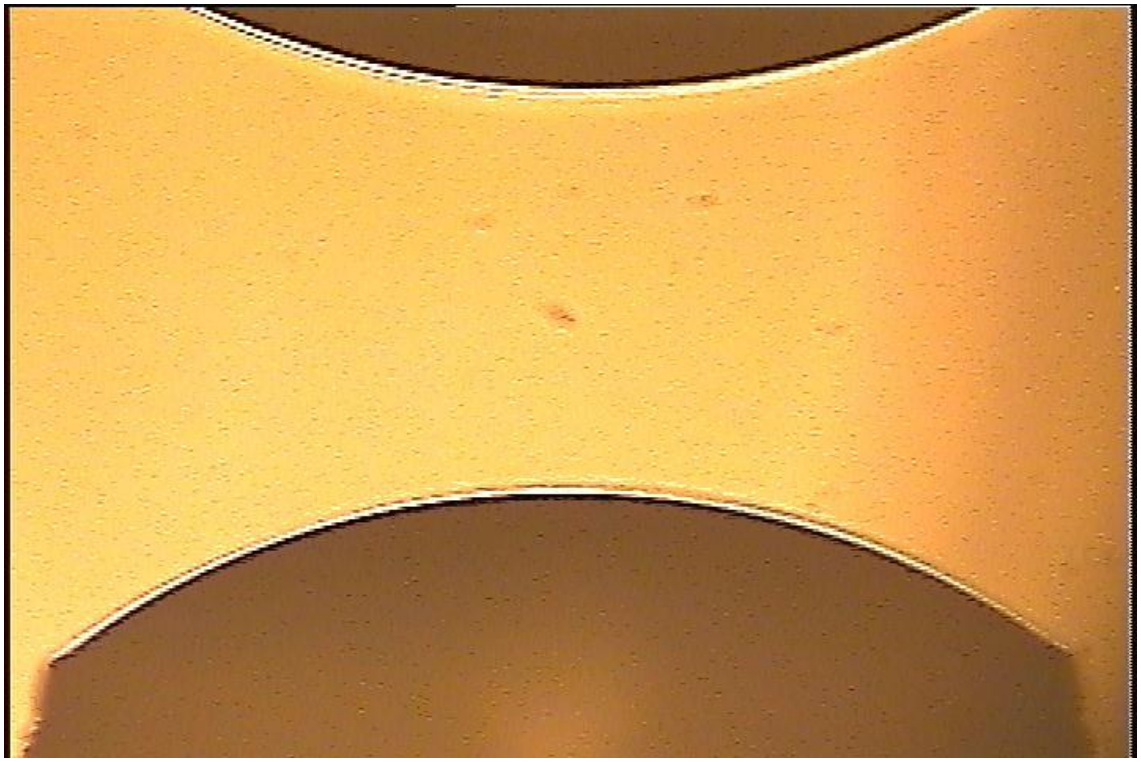

Figure 2. Optical epoxy injected into machine ferrule using capillary action.

Since the empty volume of the machined ferrule is greater than the volume of epoxy in the convex epoxy meniscus, the injection process was repeated several few times until the entire volume of the machined ferrule is filled with epoxy. Due to surface tension, a convex epoxy meniscus formed on the front of the machined ferrule. Since the NSOM probe tip must protrude outside the epoxy meniscus, the NSOM probe needed to be positioned 1-3 µm outside the surface of this convex meniscus (see Figure 3).

Figure 3. NSOM probe placed a few microns outside epoxy surface.

In order to position the NSOM aperture properly, monochromatic laser light (we use red light) was coupled into the NSOM probe in order to locate the NSOM aperture using the optical microscope. By observing the position of the laser light emitted from the NSOM aperture, the NSOM aperture was positioned 1-3 µm outside the epoxy meniscus. During positioning, red light from NSOM aperture was visible when the microscope light was turned off.

Now, the epoxy was allowed to fully cure. During curing of the optical epoxy, the epoxy volume was reduced due to epoxy shrinkage, causing the NSOM aperture to protrude from the epoxy surface. Additional epoxy was used to coat the sides of the NSOM probe which protruded outside the epoxy. A second epoxy injection rod with a smaller diameter (125 um fiber in this case) was used to apply a few pico liters of additional epoxy to the NSOM probe tip. Surface tension enabled the epoxy to flow down the exposed part of the NSOM fiber tip, encapsulating the whole fiber tip and leaving only a few microns at the very tip uncovered (see Figure 4).

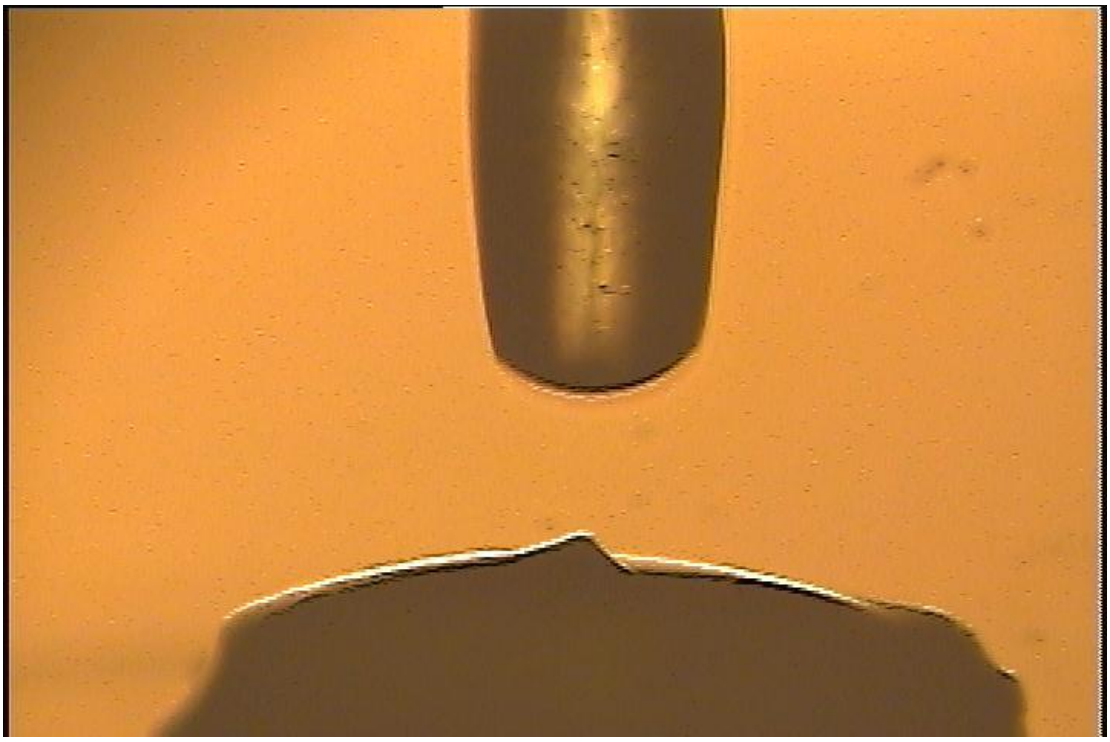

Figure 4. Additional epoxy added to coat sides of NSOM probe using second epoxy injection rod.

Figure 5a shows a conceptual diagram of a coated NSOM tip inside a fiber optic ferrule. Figure 5a shows the NSOM probe inside a ferrule before epoxy is applied. Figure 5c shows a NSOM probe after application of a small amount of epoxy. Figure 5d shows a NSOM tip which is completely coated with epoxy.

After the NSOM probe was completely covered with epoxy, the epoxy was allowed to completely cure. In order to use the NSOM probe in experiments, excess epoxy must be removed from the NSOM probe aperture. To determine the amount of excess epoxy to be removed, the NSOM probe aperture was examined using secondary electron

microscopy (SEM).

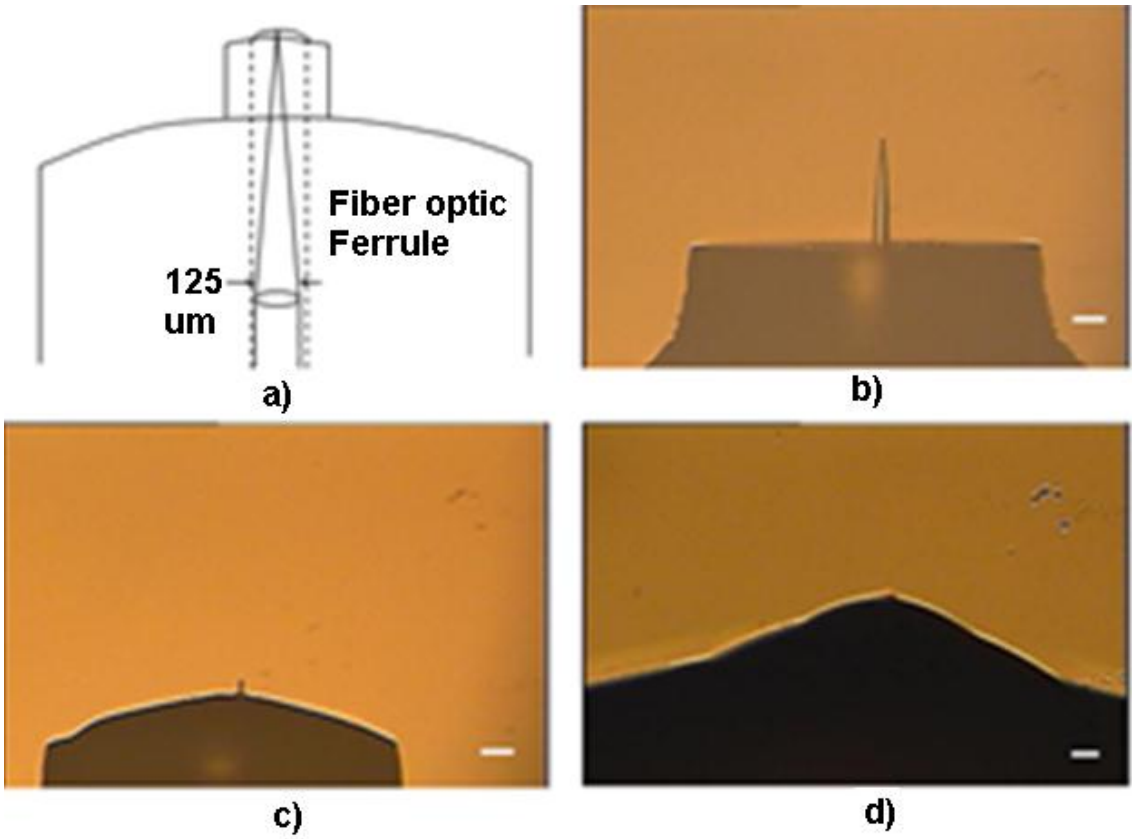

Figure 5. a) Conceptual diagram of a coated NSOM tip inside a fiber optic ferrule, b) NSOM probe inside a ferrule before epoxy is applied (scale bar is 40 μm), c) a NSOM probe after application of a small amount of epoxy (scale bar is 40 μm). d) CCD image of a NSOM tip coated with epoxy (scale bar is 10 μm). Reproduced with permission of IOP Publishing.

Figure 6a shows the amount of epoxy on the NSOM aperture. After RIE etching finished, The NSOM aperture was examined again using SEM, backscattered electron microscopy (BSE), and energy-dispersive x-ray diffraction (EDS) to ensure that excess epoxy was completely removed. The NSOM aperture after RIE etching is shown in Figure 6b. A zoomed-in view of the NSOM aperture after RIE etching is shown in Figure 6c.

From the SEM images in Figure 6a-c, it is apparent that there is no observable damage to the gold coating on the sides NSOM probe. Hence, the primary etching mechanism of the epoxy is chemical etching rather than sputtering. Also, there is no observable damage to the NSOM aperture due to sputtering, and the aperture is clearly observable.

Figure 6d shows a backscattered electron image of NSOM aperture. There is clear contrast between the epoxy and gold on the NSOM aperture. As Figure 6d shows, there is no observable excess epoxy on the NSOM aperture. Additionally, it is apparent, that there is no damage to the gold coating on the NSOM aperture. This indicates that evanescent field from the NSOM probe is still suitable for usage during experiments.

The SEM results show that this RIE procedure is able to prevent damage to the gold coating, despite the lightning-rod effect caused by the gold coating on the NSOM probe. EDS was also used to ensure the absence of epoxy on the NSOM aperture. EDS results showed no observable epoxy on the NSOM aperture.

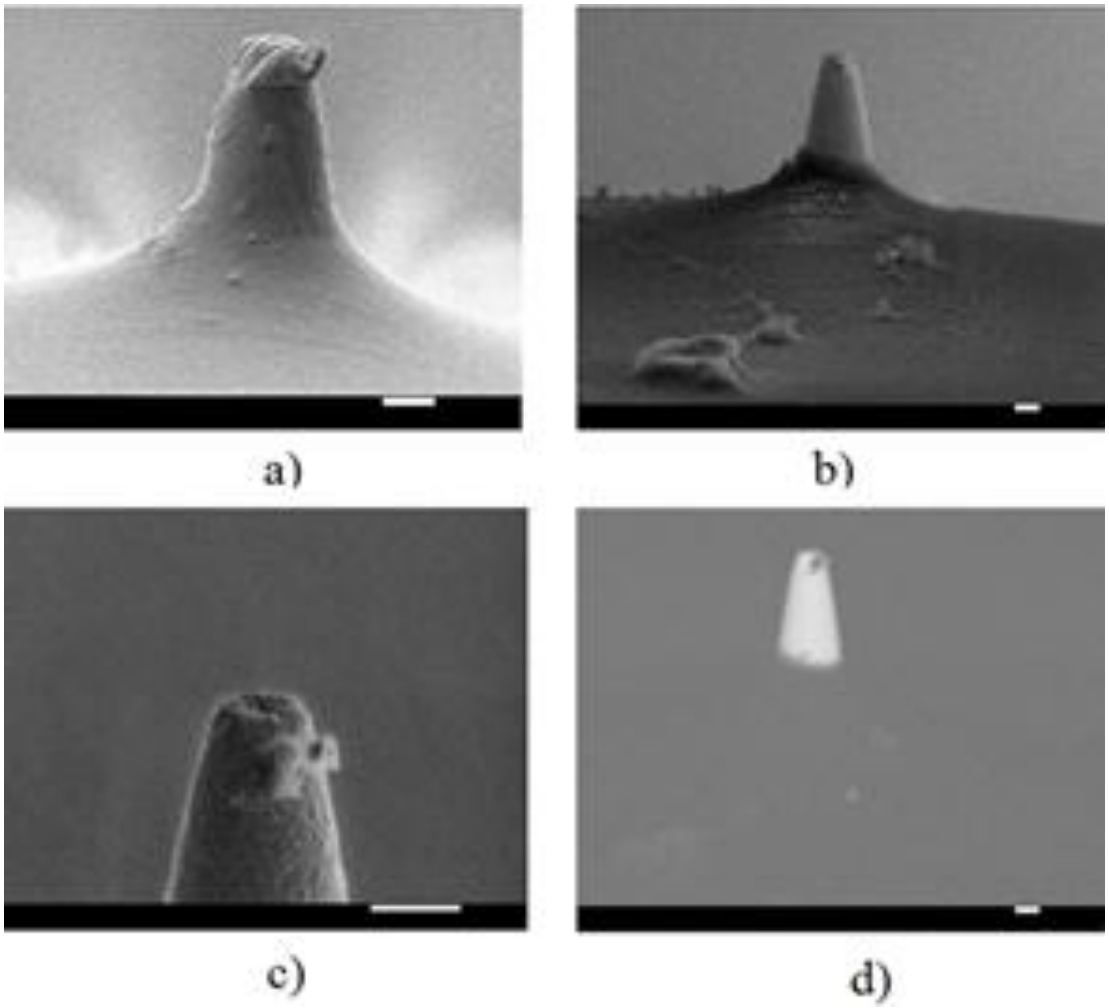

Figure 6. (a) SEM image of NSOM probe before Reactive Ion Etching. (b) SEM image of the NSOM probe after Reactive Ion Etching. (c) Zoomed-in view of the NSOM aperture after Reactive Ion Etching. (d) BSE image of the NSOM probe after Reactive Ion Etching. For all images, scale bar is 1 µm. Reproduced with permission of IOP Publishing.

Verification of NSOM probe's integrity during high power operations

In this study, the NSOM probe used was the UV NSOM probe from Nanonics, which consists of a gold-coated probe with a sub-micron aperture (100 nm). The NSOM probe was fabricated using the laser-pulling method. The input end of the NSOM probe was connectorized using a fiber optic connector. The laser was a connectorized pig-tail laser diode, with emission at 405 nm. Light was coupled into the NSOM probe by connecting both connectors. The integrity of the NSOM probe was evaluated by measuring transmitted power of the NSOM probe vs. the input laser power. The transmitted light was collected by a Thorlabs power meter, using a large area detector. The NSOM probe tip was positioned very close to the detector so that all transmitted light was collected by the detector. Since the refractive angle is 10.6^{o} (because the refractive index of silicon is 5.4 at 405 nm wavelength), the detector detects nearly all transmitted light, even if the incident angle is 90°. First, the transmitted power from the NSOM probe was measured as a function of the laser current. The NSOM probe's fiber input was then cut, but the connector was not disconnected. The laser power coupled into the NSOM fiber was determined by butting the fiber's cut end to the detector and measuring the detector power vs. laser current. The measurement was repeated three times. Figure 7 shows the overlapping data of the input power versus output power, up to an input power of 21.4 mW. The measurements were stopped at 21.4 mW to prevent damaging the laser.

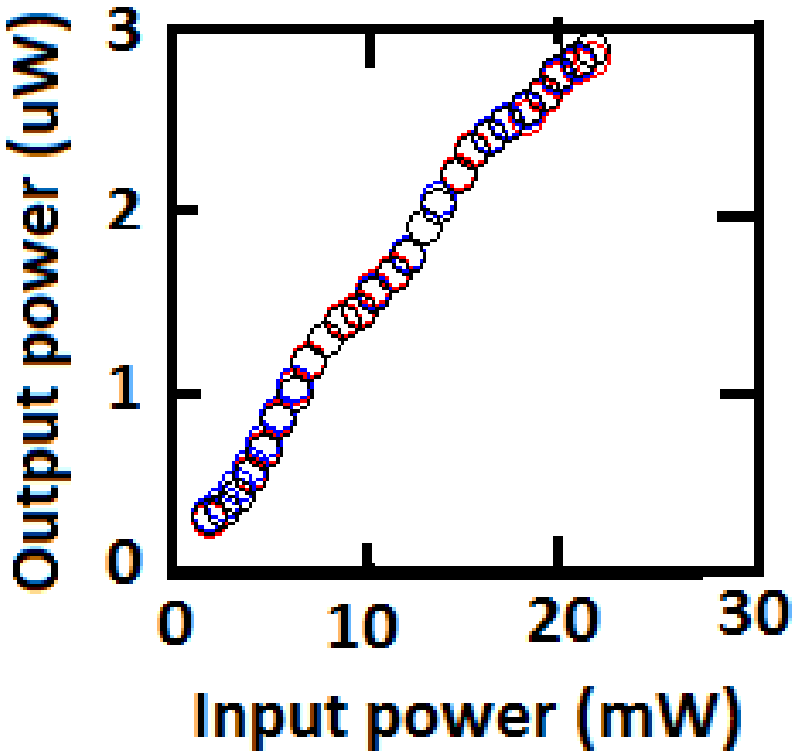

Figure 7. Plot of output power versus the input power for three measurements. Reproduced with permission of IOP Publishing.

Heating-induced damage to the NSOM probe's gold coating permanently comprises the integrity of the probe, and the output power increases significantly. Therefore, the repeatability of the data shown in Figure 7 proves that the gold coating is intact. The transmittance of the probe is 1.2×10^{-4}, which is comparable to the nominal transmittance of 5×10^{-5}, which is quoted by the vendor for the 100 nm apertured NSOM probe.

A non-defective NSOM probe should have light emission only from the aperture. So, direct light-emission imaging of the NSOM probe after higher power operation was

used to verify integrity of the NSOM probe. Imaging of the NSOM probe's emitting surface was conducted using a high numerical aperture microscope objective. An Olympus UPlanApo apochromatic objective (with NA of 0.85) was used to obtain diffraction-limited resolution. Images were recorded using a CCD camera. The emitting surface of the NSOM tip, illuminated by the white light source of the microscope, is shown in Figure 8a. Reflection from the gold coating of the emitting surface of the probe's tip is observable, and the central dark region, which is the position of the probe's aperture, is also observable. The diameter of the front surface of the NSOM probe is about 800 nm. The central dark region cannot be resolved because the aperture diameter is below the diffraction limit. Figure 8b shows the probe's surface when the laser is turned on. The center of the Airy pattern coincides with the central dark region. The spot size is approximately 320 nm, which is comparable to the diffraction limit. Figure 8c shows the emitting surface with the microscope light turned off. Figure 8d shows the Airy pattern of the light from the probe's aperture at a laser power of 21.4 mW. The emission spot was symmetric, and no additional emission regions are observable. The NSOM tip was translated towards and away from the microscope objective to determine if any additional emission regions existed, but no additional emission spots were observed. The probe was also examined using a microscope objective with a larger field of view than what is observable using the high NA objective. No additional emission spots were observable. Therefore, it is shown that there were no additional emission spots inside or outside the epoxy region, as the epoxy is transparent.

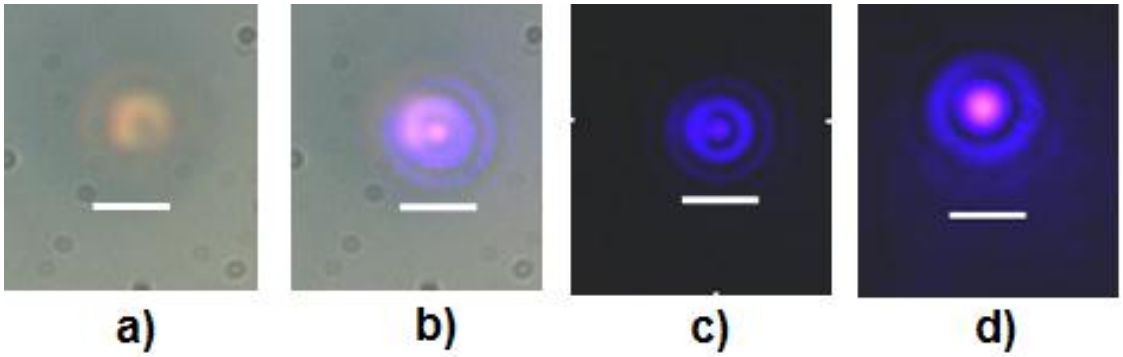

Figure 8. Image of the emitting surface of the probe tip. a) Microscope lighting only. b) microscope lighting on and laser on. c) microscope lighting off and laser on. d) image with laser power at 21.4 mW. For all images, scale bar is 1 µm. Reproduced with permission of IOP Publishing.

Summary

In conclusion, NSOM probes with epoxy heat sinks were demonstrated. The position of the epoxy was carefully controlled so that the probe's tip protrudes out of the epoxy by only 2-3 microns. SEM, EDS, and BSE were used to examine the fabricated NSOM probes to verify the integrity of the epoxied NSOM probes. Optical imaging and optical power measurements were used to verify that the NSOM probe was not damaged when 405 nm light, at an input power of 21.4 mW, was coupled into the NSOM probe.

3. NEAR-FIELD LITHOGRAPHY USING A NEAR-FIELD PROBE WITH AN EPOXY HEAT SINK

Overview

Studying samples under high magnification is important in many areas such as engineering and material science. The spatial resolution attainable with optical microscopes is limited to about half the wavelength of the light source if a high numerical aperture microscope objective is used. One approach to overcome the diffraction limit is by using Near Field Scanning Optical Microscopy. NSOM involves using a fiber probe that has an opening which is much smaller than the wavelength of the light source. When light propagates through the fiber, the majority of the light will be absorbed by the tip or reflect, but a small amount will propagate through the opening. However, the light does not propagate outside the opening. Instead, the electric field distribution outside the tip follows an exponential decay.

Theoretical description of near-field probes

For an aperture of diameter 2a, the minimum range of β_r is given by the uncertainty principle:

$$\Delta\beta r \cdot \Delta r \geq 2\pi \quad \text{or} \quad (\Delta\beta r)_{\min} = \frac{\pi}{a} \tag{1}$$

The electric field E(r,z) at the aperture is given by:

$$E(r,z) = \sum_{\sigma,\beta_x,\beta_y} E_\sigma(\beta_x,\beta_y) \cdot \exp(j\beta_z z + j\beta_x x + j\beta_y y) \tag{2}$$

From Maxwell's equations:

$$\nabla^2 E + k_0^2 \varepsilon \cdot E = 0 \tag{3}$$

$$\beta_z = +\sqrt{k_0^2 \varepsilon - \beta_x^2 - \beta_y^2} = \sqrt{k_0^2 \varepsilon - \beta_r^2} \text{ and } \varepsilon = 1 \tag{4}$$

If:

$$\Delta\beta_z \geq \frac{2\pi}{\Delta r} \geq k_0 \sqrt{\varepsilon} \rightarrow \Delta r \leq \frac{\lambda}{\sqrt{\varepsilon}} \tag{5}$$

Then, β_z becomes imaginary:

$$\beta_z = i\sqrt{\left(\frac{2\pi}{\Delta r}\right)^2 - k_0^2 \varepsilon} \tag{6}$$

With the Bethe/Bouwkamp model [21], the transmission coefficient scales as a^4, where a denotes the aperture diameter [22, 23]. However, the intensity of the evanescent field cannot be increased by increasing the intensity of the input light because the metal coating on the NSOM tip will melt when more than a few mW of power is introduced into the NSOM fiber.

Near-field Scanning Optical Lithography (NSOL) [34-38] using a NSOM probe can fabricate sub-diffraction patterns using evanescent waves. Using a sub-diffraction aperture, evanescent light exposes the photoresist layer. Although NSOL offers sub diffraction-limited resolution, it requires slow scan speeds since high input optical powers cannot be used. NSOL with heat sinks have never been used, and the intensity of the input light source has been limited to a few mW. Using a heat sink and higher input optical power will increase the scan rate.

Researchers have exposed photoresist films using NSOM probes, but the developed pattern in the photoresist did not extend through the entire photoresist layer. Naber

et. al. made a pattern in photoresist that was 78 nm wide but only 20 nm deep, and the thickness of their photoresist layer was 70 nm [39]. The triangular shape of the pattern obtained by Naber is explained by the exponential decay of the evanescent wave outside of the aperture. Figure 9 shows a Bethe/Bouwkamp calculation of the approximate evanescent intensity from a small hole in an opaque screen. Figure 10 shows the intensity versus distance from the aperture. The intensity follows an exponential decay.

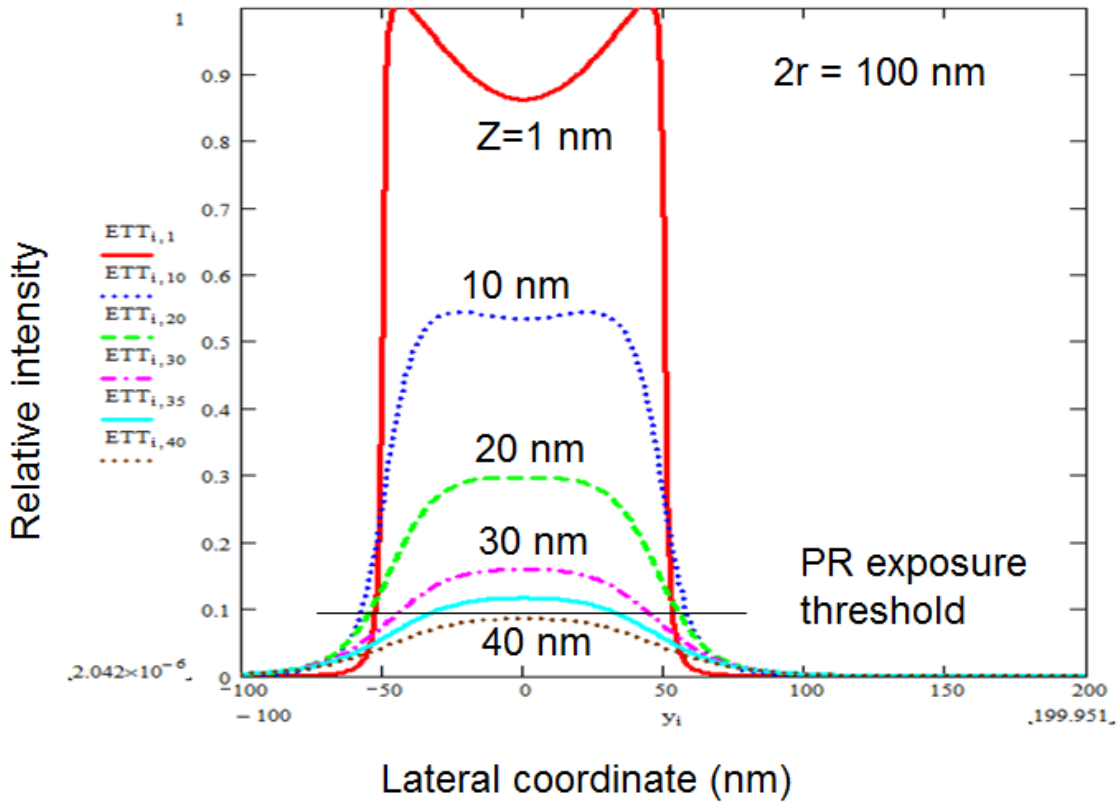

Figure 9. Bethe/Bouwkamp calculation of the approximate evanescent intensity from a small hole in an opaque screen.

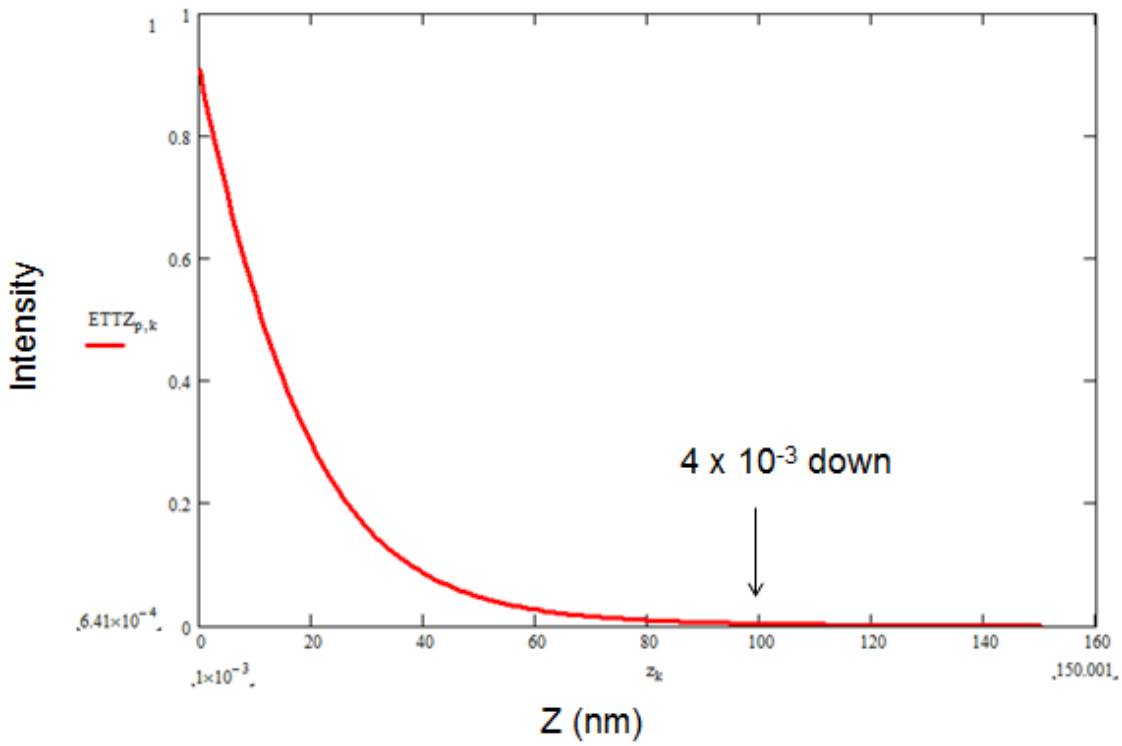

Figure 10. Intensity versus distance from the aperture

Feedback distance control for NSOM lithography

The NSOM probe tip must be held a few nanometers from the sample during scanning in order to obtain high-quality images. Several feedback mechanisms have been developed based on electron tunneling current [40, 41], photon transmission through the sample [42], and shear-force measurements [43, 44]. None of these feedback methods can be directly applied to for the experiment in this study. Electron tunneling current cannot be applied because the zirconium oxide ferrule and epoxy are both insulators, and the magnitude of the tunneling current would be very small. Photon transmission through the sample provides information about the distance between the NSOM probe and the sample,

but electron tunneling current must also be used in order to determine when the NSOM tip and sample are a few nanometers apart. Also, shear-force measurements are not compatible with NSOM tips that are coated with epoxy because the tip cannot resonate.

Therefore, novel optical distance control was developed in this research. The optical setup for tip-surface distance control is shown in Figure 11. In Figure 11, a low numerical aperture (NA = 0.16) collimates the light from a 528 nm laser. The light is first polarized by a polarization beam splitter (PBS). The green light is then split by a beam splitter BS2. Half of the green light retro-reflects off mirror M1. The other half of the green light reflects off M3 on the spring fixture. The NSOM probe is inside a fiber optic ferrule which is mounted on a platform that is attached by three low-k springs. The spring fixture is attached to an optical microscope. After reflecting off the mirror M2 on the platform, the light is recombined by BS2 and collected by a CMOS image sensor. The two optical paths combine on the CMOS image sensor, generating a fringe pattern as shown.

For distance control, the wafer is slowly moved upwards by the X-Y-Z nano-translator. The CMOS image sensor can be used for rough positioning of the z-position of the wafer. When the wafer makes contact with the NSOM tip and compresses the springs by 5 nm (or more), the mirror on the platform also moves upwards by 5 nm (or more), which causes the fringe pattern to shift observably on the CMOS image sensor. It was found that compressing the springs by as much as 100 nm still did not damage the NSOM tip, but the wafer surface is kept approximately 10 nm away from the NSOM tip during scanning to eliminate pressure on the NSOM tip. The fringe pattern shift can also be quantified by

replacing the CMOS image sensor with a photodiode. Computer software keeps the NSOM tip within 10 nm of the photoresist surface during exposure.

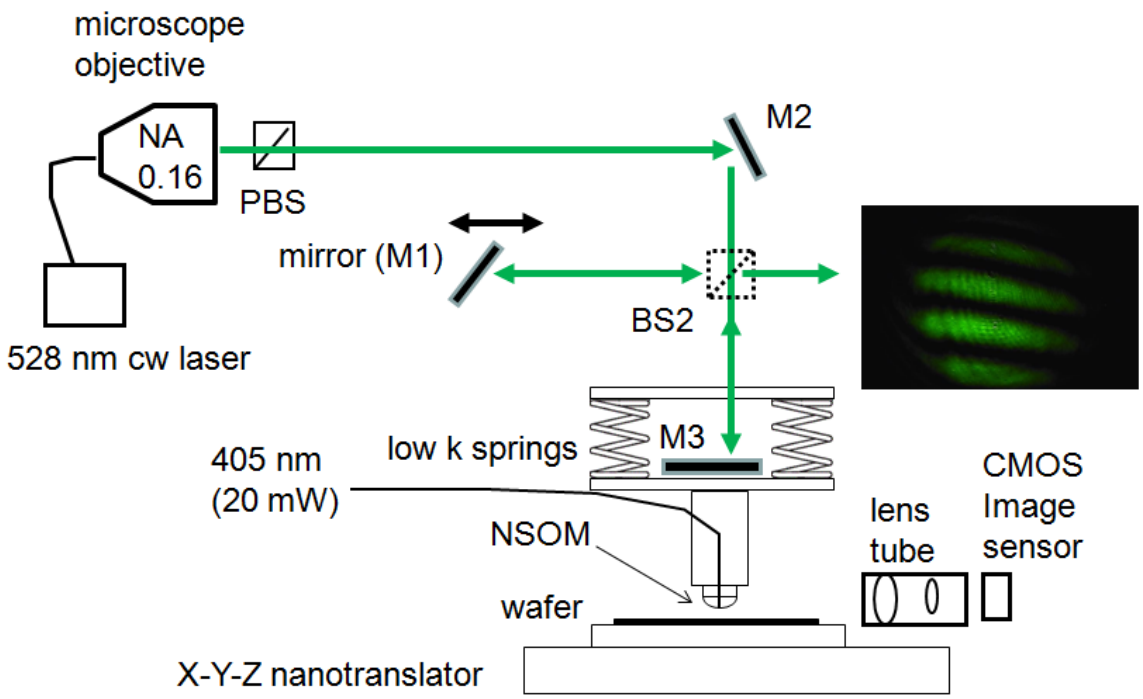

Figure 11. Optical setup for photolithography

NSOM lithography experiments

AZ5214E positive photoresist was used in this study. The photoresist film was spin-coated on a cleaned silicon wafer. First, hexamethyl disilane (HDMS) primer was deposited on the wafer. Then, the resist was diluted using Thinner P (PGMEA) by a factor of 1:6. The resist was spin coated on the silicon wafer at rotation speed of 4000 rpm. The wafer was then baked on a hot plate at 100 ºC for 60 seconds. The thickness of the film

was 93 nm, with a variation of approximately 1 nm across the wafer, as measured using a reflectometer. Laser light from a cw-laser diode, $\lambda = 405$ nm, was coupled into the NSOM probe. The NSOM tip had an aperture of about 100 nm (20º cone angle) at the tip. The throughput of this type of NSOM probe is approximately 10^{-4}. The number of pulses was controlled using computer software, and the pulse duration was controlled using an external home-built circuit. The laser diode was biased using a current source. After exposure, the sample was developed using developer AZ 400K for 10 seconds. The developer was diluted using DI water by a factor of 1:4. After development, the wafer was washed with DI water and dried with nitrogen gas. The sample was characterized using scanning electron microscopy and backscattered electrons.

In order to ascertain the dwell time needed to expose through the photoresist, the following scan scheme was employed: as the tip position moved laterally, it was programed to dwell at periodic positions for a chosen time interval. The quick spatial movement after each dwell is 20 nm, so that the exposing light spots overlap, which should result in a straight line. Different chosen dwell time intervals will correspond to different parallel rows of lines. Figure 12 shows an SEM image of parallel lines that were fabricated using NSOL. However, after photoresist development only the line that was exposed completely through the photoresist layer will show in the SEM image because of the strong contrast in the intensity of backscattered electrons between the photoresist layer and silicon wafer.

The exposure input power was 20 mW for all lines. The lines were formed by patterning dots in the photoresist with a spacing of 20 nm between adjacent dots as described above. The dots in each line were exposed using the same exposure time. In Figure 12a, the times for the four lines were 2 µs, 22 µs, 42 µs, and 62 µs per dot. Vertical spacing between adjacent lines was 500 nm.

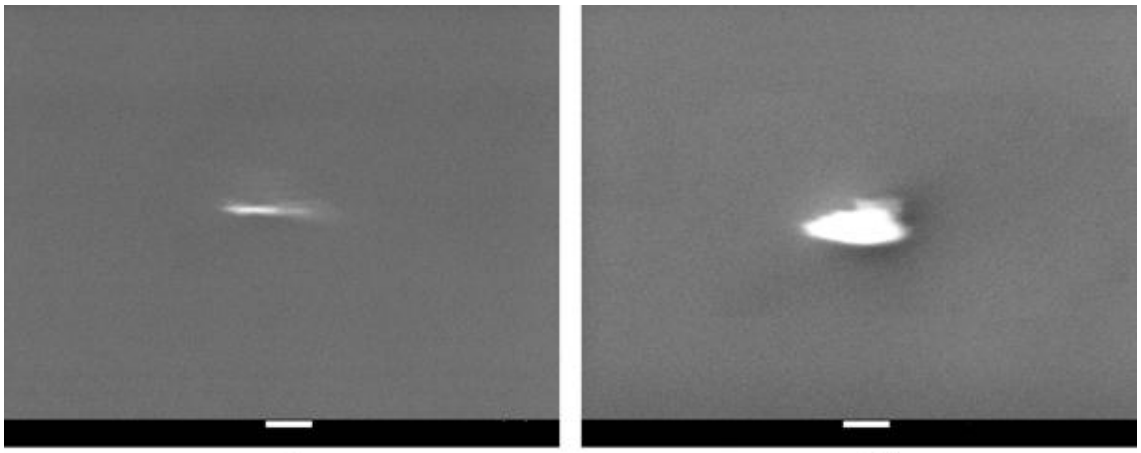

a) b)

Figure 12. Photoresist exposure using 93 nm thick photoresist with laser input power of 20 mW. (a) Lines exposed using exposure times of 2 µs, 22 µs, 42 µs, and 62 µs per dot. Only the line exposed using an exposure time of 62 µs per dot was able to expose completely through the photoresist layer. Width of the line was approximately 150 nm. (b) Lines exposed using exposure times of 100 µs, 200 µs, and 300 µs per dot. For both figures, scale bar is 1 µm.

Only the dots exposed using an exposure time of 62 μs per dot were able to expose completely through the photoresist layer. In Figure 12b, the exposure time for 100 μs, 200 μs, and 300 μs per dot. Since the minimum exposure time was only 62 μs, all of the dots fabricated in Figure 12b were over-exposed, causing the adjacent lines to merge together.

Summary

NSOL using a NSOM probe with an epoxy heat sink was demonstrated. The input optical power was increased to 20 mW (cw-laser, λ = 400 nm) without damaging the NSOM probe. The probe was used to expose though 93 nm thick photoresist at 62 μs dwell time, giving a potential line scan of about 300 μm/sec with a 100 nm NSOM probe.

4. A VERSATILE STIMULATED EMISSION DEPLETION MICROSCOPE WITH A SUPERCONTINUUM LIGHT SOURCE*

Overview

Diffraction effects limit the resolving power of an optical microscope to approximately half the wavelength of light. Confocal microscopes have a lateral resolution and axial resolution of approximately 250 nm and 500 nm, respectively, if a high NA objective is used. Stimulated Emission Depletion (STED) Microscopy breaks the diffraction limit by suppressing the florescence emitted from dye molecules via stimulated emission [46]. In STED, the excited state of the dye molecules population is depleted via the simulated emission effect [47, 48]. Recently, birefringent elements have been used to improve the resolution and simplify designs [49].

Other methods for achieving super-resolution include Saturated Patterned Excitation Microscopy (SPEM) [50], Saturated Structured Illumination Microscopy (SSIM) [51], PALM [52, 53] and STORM [54-56]. In SSIM and SPEM, the sample is illuminated by a periodic optical pattern, which is described by wave vector k_1. The spatial beat between k_1 and the k-vector space of the sample is measured. Due to saturation effects, the non-linear behavior of excited molecules decreases the r-space resolution and simultaneously increases the k-space resolution. PALM and STORM rely on sequential registration of dye molecules which are separated by a distance larger than the diffraction limit. The

* Reprinted with permission from "A low cost and versatile STED superresolution fluorescent microscope," by McBride D., Su C. B., Kameoka J., Vitha S., 2013, *Modern Instrumentation* (2), pp. 41-48, Copyright 2013 by Scientific Research Publishing

center of each dye molecules is calculated using a fitting algorithm, with an accuracy that exceeds the diffraction limit. Molecules that were previously turned off will eventually photo-bleach, reducing the likelihood of producing a mistaken molecular position. In STORM, photo-switchable molecules are switched off between each frame using a laser which has a longer wavelength [56].

Theoretical description of stimulated-emission depletion microscopy

A vortex phase plate [57] is placed in the path of a collimated depletion beam. The depletion beam is focused by a high NA microscope objective, producing a donut-shaped focal spot with a central intensity null (Figure 13a). A focused shorter wavelength excitation beam produces a fluorescent spot from dye molecules, as shown in Figure 13b.

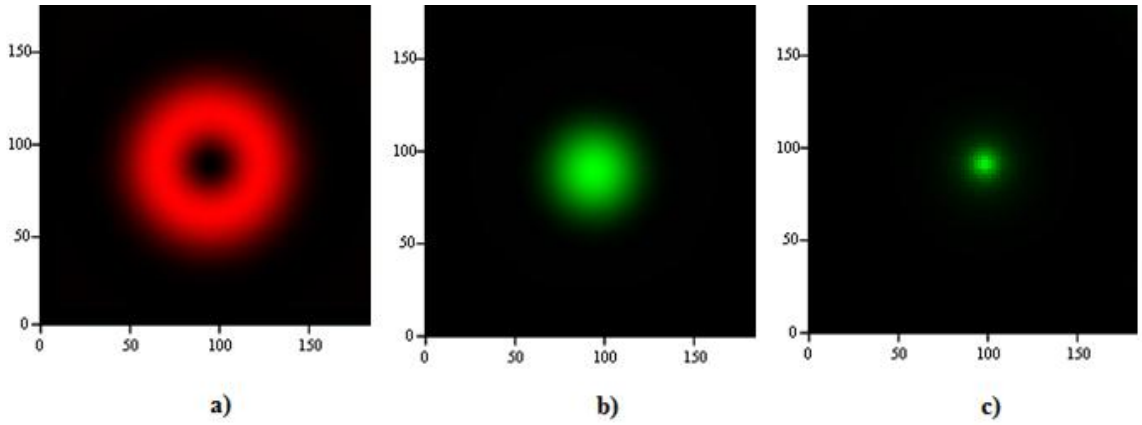

Figure 13. Basic principle of STED. a) The focal spot of a red depletion beam with a central intensity null, b) Green fluorescence due to dye molecules which are excited by a focused excitation beam, and c) Resultant emission spot. The size of the image frame is 2 x 2 μm.

The fluorescent intensity is directly proportional to the fluorophore excited state population. When the excitation and depletion beams overlap, the excited dye molecules which reside outside the central intensity null are de-excited to the ground state by the depletion beam via the stimulated emission effect. The size of the resulting emission spot is decreased, as in Figure 13c.

Here, the general formulas for calculating resultant emission spot are described. The result of reference [58] is extended by including the effect of phase plates which are placed in the object plane of a microscope. Also, a Gaussian wave is used, rather than a plane wave.

The positive z direction is the axial direction of the microscope objective lens through the center of the lens and away from the image plane. Using spherical coordinates, a point in the image plane is defined by coordinates (R, Θ, Φ). Then, a common function to be used is:

$$K(R,\Theta,\Phi,\theta,\phi) = exp\{ik_0 \cdot [R \cdot (cos(\theta) \cdot cos(\Theta) + sin(\theta) \cdot sin(\Theta) \cdot cos(\phi - \Phi))]\} \quad (7)$$

where, $k_0 = 2\pi \cdot n / \lambda$, n is the refractive index of the immersion medium of the objective, and λ is the wavelength. Φ and θ are variables of integration.

With incident light which is polarization in the x-direction, the x, y, and z components of the electric field at any point in the image plane are described by,

$$E_x = \int_0^{\alpha} \int_0^{2\pi} G_x(\theta,\phi) \cdot K(R,\Theta,\Phi,\theta,\phi) \cdot F_\phi(\phi) \cdot F_\theta(\theta) \cdot d\phi \cdot d\theta \quad (8a)$$

$$E_y = \int_0^{\alpha} \int_0^{2\pi} G_y(\theta,\phi) \cdot K(R,\Theta,\Phi,\theta,\phi) \cdot F_\phi(\phi) \cdot F_\theta(\theta) \cdot d\phi \cdot d\theta \quad (8b)$$

$$E_z = \int_0^{\alpha}\int_0^{2\pi} G_z(\theta,\phi)\cdot K(R,\Theta,\Phi,\theta,\phi)\cdot F_\phi(\phi)\cdot F_\theta(\theta)\cdot d\phi\cdot d\theta \tag{8c}$$

where G_x , G_y , and G_z are given by,

$$G_x = -\sqrt{cos(\theta)}\cdot sin(\theta)\cdot\{cos(\theta)+[1-cos(\theta)]\cdot sin^2(\phi)\} \tag{9a}$$

$$G_y = \sqrt{cos(\theta)}\cdot sin(\theta)\cdot\{[1-cos(\theta)]\cdot sin(\phi)\cdot cos(\phi)\} \tag{9b}$$

$$G_z = \sqrt{cos(\theta)}\cdot sin^2(\theta)\cdot cos(\phi) \tag{9c}$$

The θ integration limit, α, is given by,

$$\alpha = sin^{-1}\left(\frac{NA}{n}\right) \tag{10}$$

where NA is the numerical aperture of the microscope objective.

$F_\Phi(\Phi)$ and $F(\theta)$ describe the effect of the phase-plate which is placed in the object space. For a first-order vortex phase plate,

$$F_\phi(\phi) = e^{i\phi} \tag{11a}$$

For a Gaussian intensity distribution without a θ-dependent phase plate,

$$F_\theta(\theta) = exp\left[-\left(\frac{D\cdot n}{2NA}\right)^2\cdot sin^2(\theta)/2\sigma^2\right] \tag{11b}$$

where D is the aperture diameter of the objective at its back focal plane, and $\sigma^2 = W^2/(4\ln(2))$. W is the half-intensity width of the collimated beam entering the microscope objective.

With incident light polarization in the y-direction, E_x, E_y, E_z are the identical as 10a-10c, but G_x, G_y, and G_z are given by,

$$G_x = \sqrt{cos(\theta)}\cdot sin(\theta)\cdot\{[1-cos(\theta)]\cdot sin(\phi)\cdot cos(\phi)\} \tag{12a}$$

$$G_y = -\sqrt{cos(\theta)} \cdot sin(\theta) \cdot \{cos(\theta) \cdot sin^2(\phi) + cos^2(\phi)\} \tag{12b}$$

$$G_z = \sqrt{cos(\theta)} \cdot sin^2(\theta) \cdot sin(\phi) \tag{12c}$$

If the incident light has equal polarization magnitudes in the x and y directions, then the intensity profile, I, near the focus is given by,

$$I = \left|\vec{E}_1 + exp(i\pi/2) \cdot \vec{E}_2\right|^2 \tag{13}$$

Here $\vec{E}_1$ is the vector sum of the electric field at the image plane (8a-8c) due to the x component of the incident electric field. $\vec{E}_2$ is the vector sum due to the y-component of the incident electric field. $\exp(i\pi/2)$ Is the phase factor which accounts for the phase shift between $\vec{E}_1$ and $\vec{E}_2$ due to the quarter wave plate.

The depletion effect of the dye molecules can be predicted by the rate equations which describe transitions between ground and excited molecular states. The absorption and emission cross-sections describe these molecular states. Since a dye molecule's energy state consists of singlet and triplet states, exact rate equation description is not realistic. For qualitative description, absorption cross-section σ_{12} and emission cross-section σ_{21} are assumed. Additionally, it is assumed that the ground and excited states have molecular density which consists of the sum of all the states in its manifold. The results shown in Figure 1c use these assumptions.

The excited state population, N_2, is described by the following rate equation,

$$\frac{dN_2(r,t)}{dt} = \left[\sigma_{12}(\lambda_e) \cdot \frac{P_e(r,t)}{h\upsilon_e}\right] \cdot N_1(r,t) - \left[\sigma_{21}(\lambda_D) \cdot \frac{P_D(r,t)}{h\upsilon_D} + \frac{1}{\tau}\right] \cdot N_2(r,t) \tag{14}$$

$$N_1(r,t) = N - N_2(r,t) \tag{15}$$

where N_1 is the ground state population. N is the total molecular density. τ is the spontaneous lifetime. λ_d and λ_e are the depletion and excitation wavelengths, respectively. Their corresponding frequencies are υ_d and υ_e. $\sigma_{12}(\lambda_e)$ and $\sigma_{21}(\lambda_D)$ are the absorption and emission cross-sections, respectively, at the excitation and depletion wavelengths. $P_e(r,t)$ is the excitation power. $P_D(r,t)$ is the depletion power. Their spatial dependence is calculated from the previously given formulas above. The powers are time-dependent because the laser is pulsed. Since the cross-section of dye molecules is approximately $1x10^{-16}$ cm^2, this value was used for σ_{12} and σ_{21}. The image of Figure 13c is obtained by solving (14)-(15), with the spatial intensity given by $\sum_t N_2(r,t)$.

Optical setup for STED microscopy

The absorption and emission spectra of the dye molecules used in this study determine the transmission and reflection spectral characteristics of the optical components which are implemented in this research. For experiments, Invitrogen F8800 (100 nm diameter) orange fluorescent beads were used for verification of super-resolution. The absorption and emission spectra of these beads is used for explaining the design of the STED microscope. In Figure 14, the absorption and emission spectra of F8800 beads is presented.

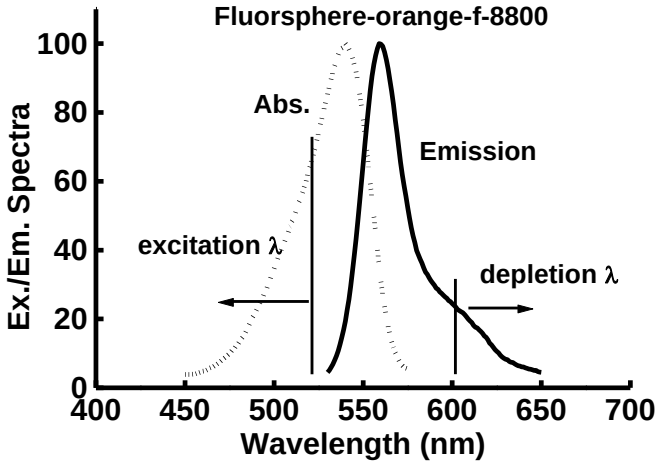

Figure 14. The extinction (absorption) and emission spectra of F8800 beads.

In Figure 15, the optical configuration of the STED microscope is presented. A low NA apochromatic microscope objective is used to collimate the light from the fiber output of a supercontinuum white light source. In this research, the Koheras SuperK Compact supercontinuum white light source was used. A higher power supercontinuum has been used for STED by other researchers [59]. The SuperK Compact outputs white light with a pulse width of 2 ns at a repetition rate of 25 kHz. A polarization beam splitter (PBS) is used to polarize the light. In order to produce a focal spot with a central intensity null, polarized light must be used with the vortex phase plate and the quarter-wave plate.

After the PBS, the white light is filtered by 561/13 nm notch filter. This notch filter passes all wavelengths of light, except the selected wavelength range within the notch. Wavelengths which are removed by this notch filter cover the fluorescence wavelength range which is detected by the photo multiplier tube. The selected wavelength range for

emitted (fluorescent) light is 9 nm, centered at 563 nm. This wavelength range is between the vertical lines shown in figure 2, and this range should be away from the excitation and depletion wavelengths.

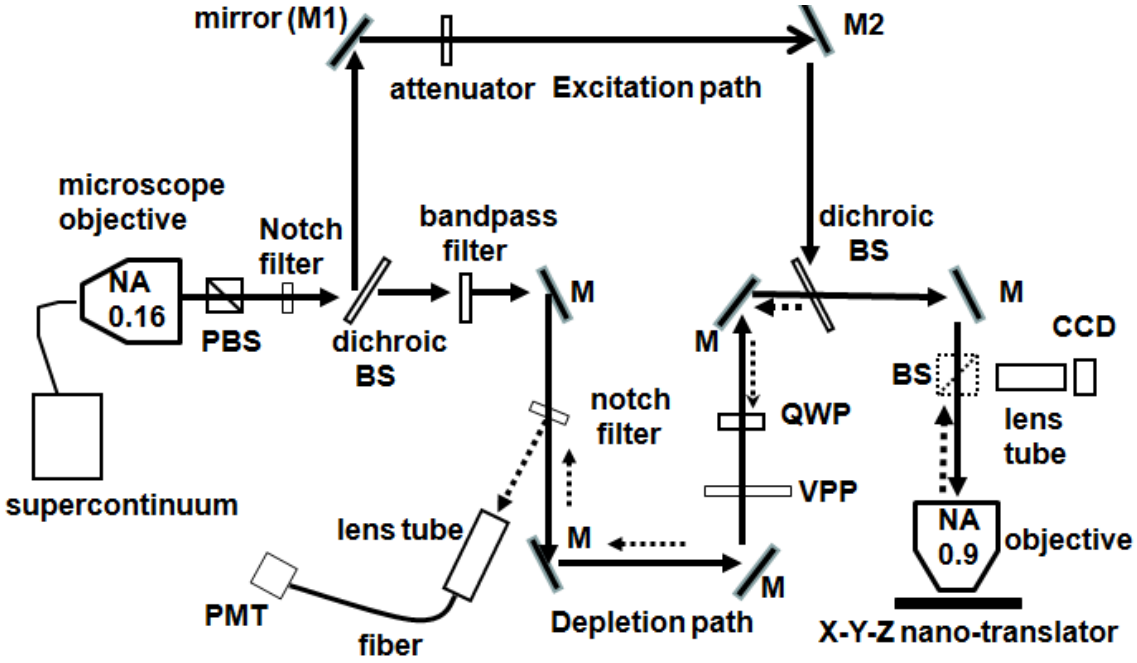

Figure 15. Design of the STED microscope used in this research. PBS: polarization beam splitter, VPP: voltage phase plate, M: mirror, BS: beam splitter, PMT: photomultiplier, QWP: quarter wave plate. Reproduced with permission of Scientific Research Publishing.

After the notch filter, the light beam is split by a dichroic beam splitter. Short wavelength light below 532 nm is reflected, and the rest of the longer wavelength is transmitted. The reflected shorter wavelength light is used for pumping the F8800 beads to their excited states for emission of fluorescent light. The power level of the Koheras

SuperK Compact light source drops off for wavelengths below 500 nm, but the shorter wavelength light still has average power of approximately 0.3 mW. This power level needs to be attenuated by a factor of 100, in this case, because average power levels above a few μW saturates the dye molecules' excited state population, with no increase in emitted light beyond a few μW. Therefore, excessive excitation power decreases the depletion effect, reducing the resolution of the microscope.

The light that is transmitted through the dichroic filter is filtered by a bandpass filter which is centered at 628 nm, with a passband width of 32 nm. The transmitted light is used for depleting the excited dye molecules. A wider passband increases the depletion power, improving the resolution. However, the width of the passband is limited by two criteria. First, as figure 2 shows, the absorption extends into the longer wavelength region of the emission spectra. Therefore, the dye absorption within the passband must be negligible. Second, the passband should not be too broad; otherwise, the central intensity of the depletion spot will not be null intensity. The notch filter which follows the bandpass filter is identical to the previous notch filter. It transmits all the light which passes through the bandpass filter, but it reflects the detection wavelength band which comes from the fluorescent emission. The vortex phase plate (VPP) and subsequent quarter-wave plate shape the beam, and the beam's cross-section exhibits a central intensity null upon focusing by the apochromatic objective with NA = 0.9. The central intensity null is caused by the cancellation of the z-component of the electric field at the focal plane, as described in reference [60] using the formula from reference [58].

The spatial resolution increases with depletion power [61]. So, one would like to

use the highest depletion power available. However, the vortex phase plate's performance is wavelength-dependent. In this study, the average depletion power is 0.9 mW.

The excitation and depletion light recombine collinearly at the second dichroic beam splitter. The combined beam is reflected downward by a mirror and focused onto the sample using a microscope objective which is mounted on the turret of the Olympus model MX 50A-F microscope. The excitation and depletion focal spots are overlapped by adjusting mirrors M1 and M2. Since the excitation and depletion spots must overlap, this places a tight constraint on tolerable beam-angle shift when components need to be changed for different dyes. The angular tolerance is approximately 3 arc-second for a 50 nm lateral shift at the image plane.

Fluorescent light from the sample is collected by the microscope objective, and it propagates backward. The dashed line shows its path. The fluorescent light from the sample retraces the original transmission path to the notch filter. It is then reflected into the lens tube and then focused into a multimode fiber and measured by the photo multiplier tube (PMT). A 563/9 nm bandpass filter (not shown) is placed inside the lens tube. An Olympus WSLM apochromatic water immersion objective (NA = 0.9) was used for evaluating the super-resolution.

A beam splitter (BS) was placed before the microscope objective, and it was used with the lens tube and the CCD camera to view the sample and monitor the overlapping focal spots. Imaging is performed by translating the sample. The sample was translated using the Melles Griot nano-translator model NanoMax 17Max600/L, with 10 nm resolution. The nano-translator and PMT were controlled using LabView programs.

All components mentioned previously, except for the PMT and the supercontinuum light source, were secured to a common platform. This platform replaced the original lens tube platform on the Olympus MX 50 microscope (Figure 4). Any light source which has a fiber connector output can be connected to the 0.16 NA objective on the platform. So, the system functions like a confocal microscope. The microscope is shown in Figure 16. The components used in the design are summarized in Table 1.

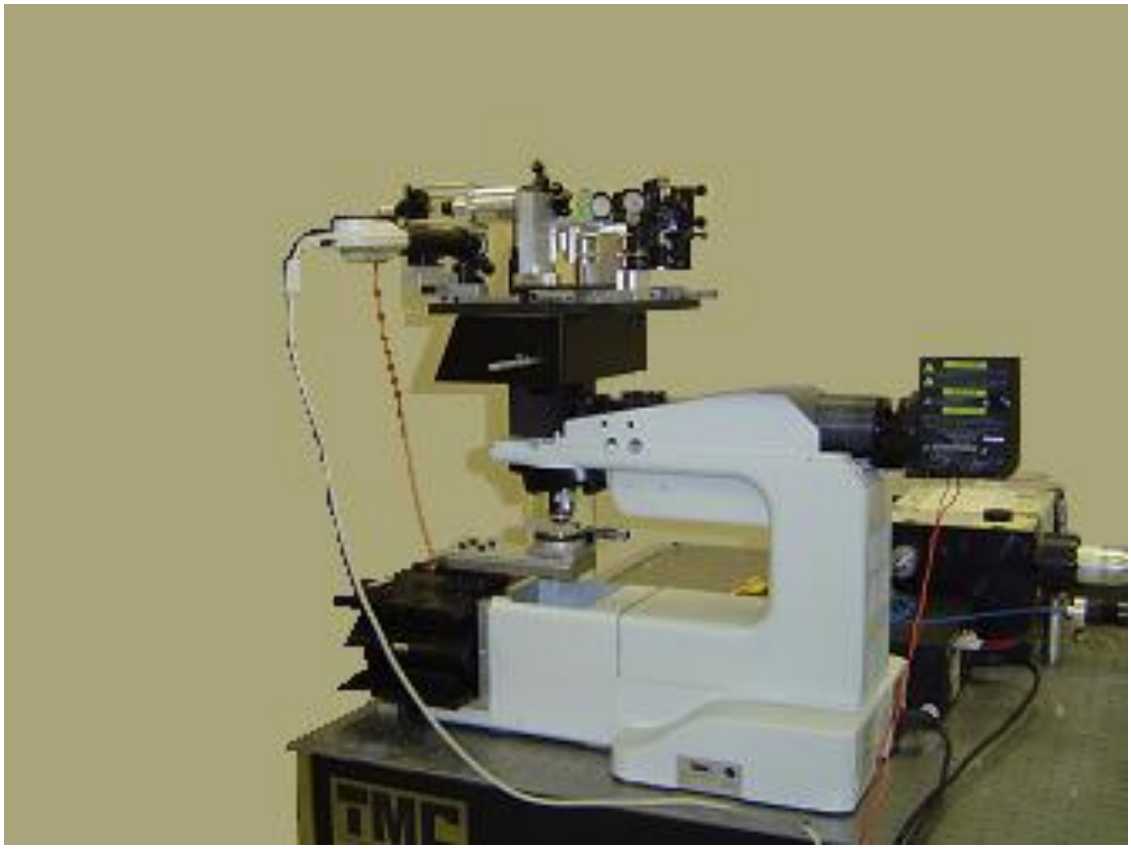

Figure 16. The STED microscope used in this research. Reproduced with permission of Scientific Research Publishing.

Table 1. Components used in the versatile STED microscope

Components	**Make**	**Model number**
Supercontinuum light source	Koheras	SuperK compact
apochromatic objective	Olympus	UPLSApo 4x/0.16
Apochromatic objective	Olympus	PlanApo 40x/0.9 WLSM
notch filters	Semrock	FF03-561/13
dichroic beamsplitter	Semrock	Di01-R532
bandpass filters	Semrock	FF01-628/32
Bandpass filters	Semrock	FF01-563/9
vortex phase plate	RPC Photonics	VPP-1
achromatic quarter waveplate	Thorlabs	AQWP05M
broadband dielectric mirrors	Thorlabs	BB1-E02
precision kinematic mirror mount	Thorlabs	KS2D
nano-translators	Melles Griot/Thorlabs	Max603D

STED microscopy experiments

To obtain super-resolution, the donut-shape focal spot from the depletion beam should have a central intensity null. The central intensity null occurs due to the cancellation of the z-component of the electric. The quality of the central intensity null cannot be evaluated by simply observing the focal spot with the CCD camera because the image spot

is not focused at the camera, and the z-component is too small. Therefore, the central dark region which is observed on the camera does not guarantee a sufficiently dark central region.

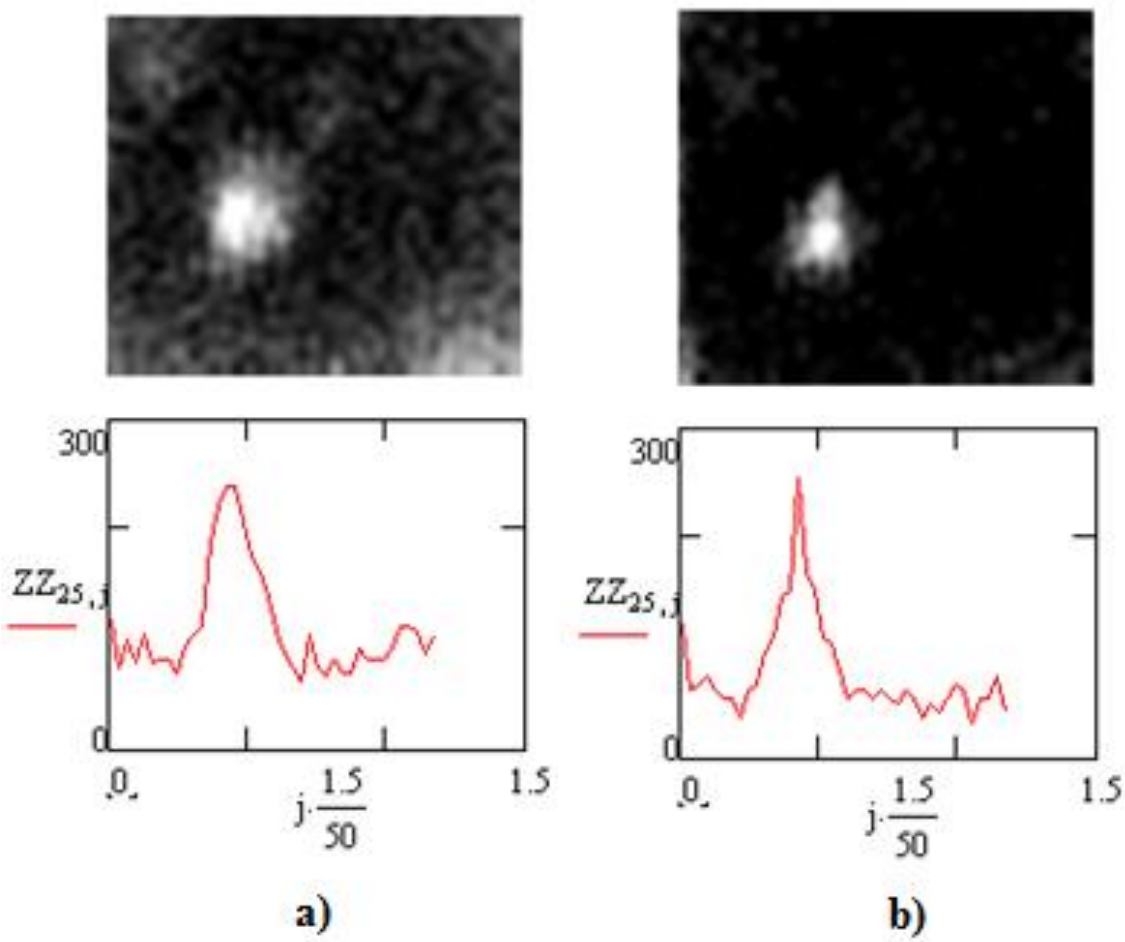

Figure 17. (a) 3μm x 3μm scan of beads with depletion beam obstructed. (b) Same scan as (a) with depletion beam unobstructed, revealing two clumps of beads. Bottom graphs show horizontal line scans through the fluorescent spots indicated in the images above.

The resolution of the microscope was measured using 100 nm F8800 fluorescent beads. The beads were embedded in agarose gel on a microscope slide and attached to a cover glass slip. The sample was translated during scanning using the nano-translator. Figure 17a shows a fluorescent image with the depletion beam obstructed. Figure 17b shows a fluorescent image with the depletion beam unobstructed, revealing two clumps of beads.

From these two graphs, it is apparent that the maximum intensity remains the same, with or without the depletion beam obstructed. When the depletion beam is unobstructed, only the width of the spot decreases because the depletion beam has a central intensity null. Using a 0.9 NA microscope objective, a convoluted later super-resolution of 90 nm is obtained, accounting for a bead diameter of 100 nm.

Summary

A versatile STED fluorescent microscope, with a configuration appropriate for using excitation and depletion beams from any supercontinuum light source, was described. The components of the microscope were placed on standard microscope frame. The collinear depletion and excitation beams were focused by a 0.9 NA microscope objective, producing a 90 nm de-convoluted lateral super-resolution, which was verified by imaging 100 nm diameter beads.

5. MEASUREMENT OF THE DEPLETION BEAM OF A STIMULATED EMISSION DEPLETION MICROSCOPE USING A NEAR-FIELD PROBE*

Overview

Scanning electron beam lithography is commonly used for nanoscale patterning, but the sample must be in a vacuum environment [62]. Lithography can be performed in air using photons, but the spatial resolution is diffraction-limited. Photo-induced activation and deactivation of polymerization using two wavelengths of light [63-67] can overcome the diffraction limit. Photopolymerization which is induced within the perimeter of a focal spot is inhibited by a second overlapping focal spot which has a central intensity null. This causes polymerization to occur only at the sub-diffraction focal spot. A second method is absorbance modulation, which uses a layer of photochromic molecules which are on a layer of photoresist. The photochromic molecules switch between two isomeric forms by exposure to two wavelengths of light [68-72]. STED fluorescent microscopy also requires a doughnut-shape depletion beam with a central intensity null [73].

Activation/deactivation photolithography and STED microscopy both require the precise measurement of the focal spots of both wavelengths. Traditionally, this measurement was performed by imaging the scattered light off a gold nanoparticle or fluorescent bead [74, 75]. However, precise localization of the nanoparticle or fluorescent bead is challenging, and assuring that scattered light originates only from the nanoparticle is also

* Reprinted with permission from "Measurement of the depletion beam focal spot using near-field scanning optical microscopy probes" by McBride D., Su C. B., 2013, *Meas. Sci. Technol.* (24) 125204, Copyright 2013 by IOP Publishing

challenging. In this study, it was demonstrated that a NSOM probe can be raster-scanned across the focal spot, providing sufficient detected light intensity to produce an image of the focal spot. The NSOM probe was inserted into a fiber optic ferrule (as previously described) for mechanical protection. Also, since the NSOM probe tip emits light, the NSOM probe tip can be easily aligned to the focal spot using an upright microscope. Therefore, this approach offers better repeatability and control and is less time-consuming than the traditional method.

Other research groups have demonstrated the use of NSOM probes for imaging. For example, three-dimensional mapping of the intensity distribution was performed using collection-mode NSOM at the focal spot generated by a high NA objective [76, 77] and studies have also been performed by measuring scattering from a sharp tip [78]. Collection-mode NSOM was also used for electric field measurements via photon tunneling caused by probe-evanescent standing-wave interaction [79]. Collection-mode NSOM has also been used for measuring wave-guide devices [80], surface-emitting laser diodes [81], and quantum wire lasers [82].

Optical setup for measurement of focal spot

Figure 18 shows the optical setup which was used to demonstrate the NSOM probe's capability to image the focal spot. The white light from a supercontinuum light source was collimated using a 0.16 NA infinity corrected UPLSAPOx4 Olympus apochromatic microscope objective. The supercontinuum light source has a photonic crystal fiber output, and the spot size is approximately the diameter of the core region of the photonic crystal fiber, which is 3.5 microns.

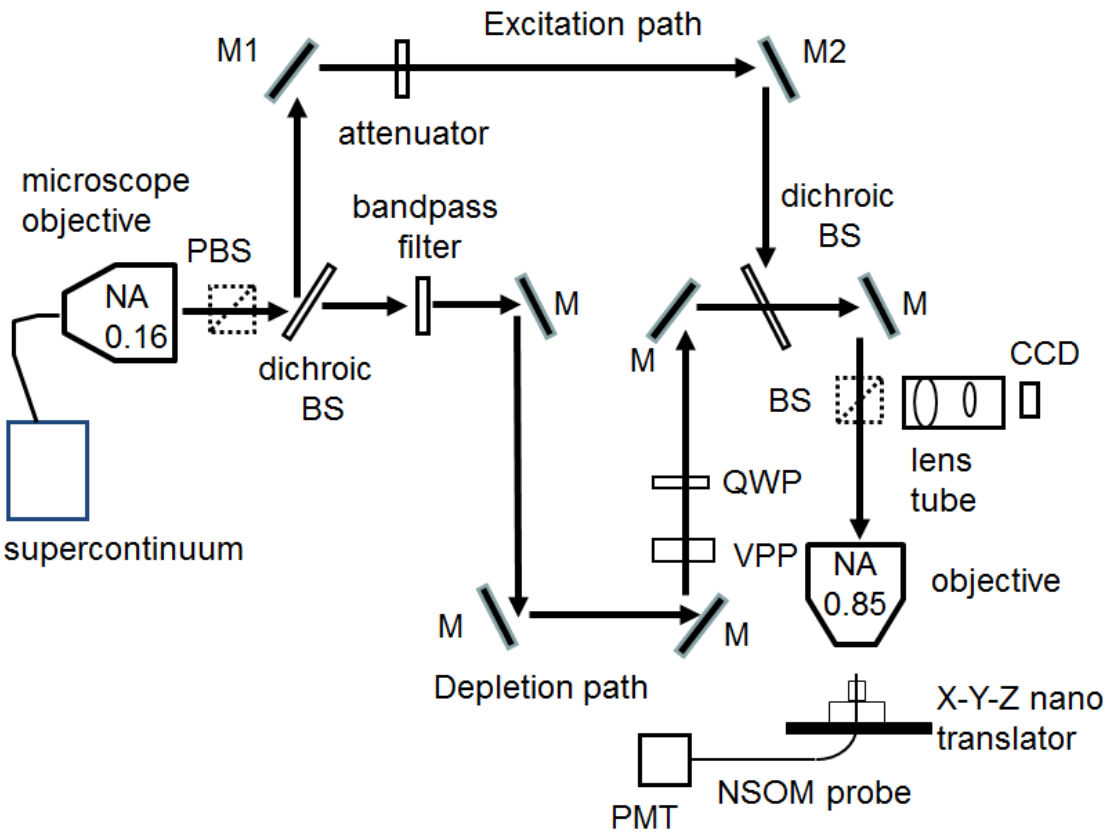

Figure 18. Optical setup for producing and measuring the doughnut shape depletion beam. PBS: polarization beam splitter, BS: beam splitter, M: λ/10 mirrors, VPP: Vortex phase plate, QWP: quarter wave plate. Reproduced with permission of IOP Publishing.

The light was first polarized using a polarization beam splitter (PBS). Polarized light is necessary because due to the vortex phase plate and quarter-wave plate which produce a focal spot with a central intensity null. The light that transmits through the dichroic filter (functional if an activation beam is used) was filtered using a 628/32 nm bandpass filter. The beam then proceeds to the vortex phase plate and quarter-wave plate.

The beam eventually reflects downward by a mirror and is focused by an infinity corrected Olympus UPlanx40 apochromatic microscope objective (NA = 0.85).

Table 2. Components used in the measurement of the focal spot

Components	**Make**	**Model number**
Supercontinuum light source	Koheras	SuperK compact
apochromatic objective	Olympus	UPLSApo 4x/0.16
apochromatic objective	Olympus	UPlanx40 0.85 NA
notch filters	Semrock	FF03-561/13
dichroic beamsplitter	Semrock	Di01-R532
bandpass filters	Semrock	FF01-628/32
Bandpass filters	Semrock	FF01-563/9
vortex phase plate	RPC Photonics	VPP-1
achromatic quarter waveplate	Thorlabs	AQWP05M
broadband dielectric mirrors	Thorlabs	BB1-E02
precision kinematic mirror mount	Thorlabs	KS2D
nano-translators	Melles Griot/Thorlabs	Max603D
NSOM probes	Nanonics	100 nm UV

The average power after the microscope objective was 0.2 mW. The CCD camera was used to facilitate alignment of the NSOM fiber probe with the focal spot. The NSOM probe was mounted on a nanotranslator with the NSOM tip point upwards. The vortex phase plate and quarter-wave plate shaped the polarized beam. After focusing by the microscope objective, the beam's cross-section should have a doughnut shaped central intensity null, as described in reference [74]. Since central intensity null is caused by the cancellation of the z-component of the electric field at the focal plane, the beam should be tightly focused. The components used in experiment are given in Table 2.

Measurements of focal spots using NSOM probes

Apertured NSOM fiber probes with an aperture diameter of 100 nm can be used for imaging the focal spot. The apertured NSOM fiber probes from Nanonics are coated with a thin layer of gold on the sides and face of the tip. As previously described in chapter 2, the NSOM fiber probe was inserted into a standard fiber optic ferrule. The ferrule was mechanically attached to the nano-translator. Since the NSOM tip is coated with gold, focused light reflects from the probe's tip, facilitating alignment of the probe tip to the focal spot. For alignment of the NSOM fiber tip with the focal spot within the CCD camera's field of view, another light source was coupled into the NSOM fiber so that both light spots could be observed using the CCD camera. To obtain an image of the focal spot, the input end of the NSOM probe was connected to a photo multiplier tube (PMT), as shown in Figure 18. A raster scan with nano-translator was then performed, and Labview software was used to synchronize the nano-translator with the output from the PMT.

Figure 20a shows a 2x2 μm scan of the focal spot obtained by raster scanning the NSOM fiber tip. The central intensity null of the depletion beam is clearly observable. An Airy ring is visible. Also shown is the horizontal line plot of the intensity profile across the central region. The intensity at the center is approximately zero. The graph on the right is the calculated focal spot profile accounting for the effect of the vortex phase plate using the image field formulas from reference [58] with the laser wavelength, microscope objective NA, microscope objective back focal plane diameter, and the collimated beam dimensions as input parameters. The electric field within the probe's aperture was summed before taking the magnitude to calculate the intensity. The calculated profile agrees well with the measured results.

Here, the details of this calculation and the parameters used are described. Using equations in chapter 4, the total electric can be written as,

$$E = E_1 + \exp(i\pi/2) \cdot E_2 \tag{16}$$

where $\vec{E}_1$ is the vector sum of the electric field at the image plane due to the x-component of the incident electric field. $\vec{E}_2$ is the vector sum due to the y-component of the incident electric field. The phase factor, $\exp(i\pi/2)$, accounts for the phase shift between $\vec{E}_1$ and $\vec{E}_2$ due to the quarter wave-plate.

In accordance with reference [83], the sum of the electric field, $\sum E$, over the aperture region is considered and calculated before calculating the intensity I = $\left|\sum E\right|^2$. The input parameters used in this calculation are: λ = 628 nm, NA = 0.85, D = 7.65 mm, and σ = 1.65 mm. D is obtained from the specification of the objective, and σ is obtained

by fitting the function $\exp\left(-X^2/2\cdot\sigma^2\right)$ to the experimental curve. The curve was measured by scanning a regular single mode fiber across the cross-section of the collimated beam in the objective plane of the microscope objective. Figure 19 shows the fitted curve and the measured data.

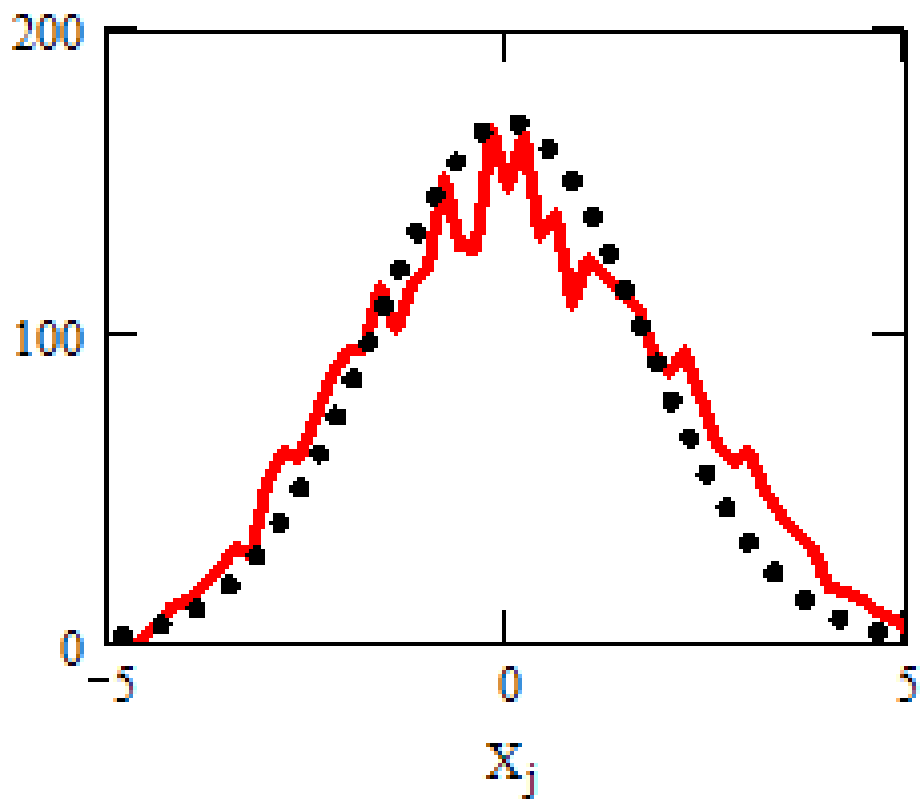

Figure 19. The line is the measured data and the dots are the fit using $\exp\left(-X^2/2\cdot\sigma^2\right)$ with σ the fitting parameter. The x-axis is in units of mm.

According to reference [83], the spatial Fourier profile of the transfer function which represents the coupling between the plane wave decomposition component of the captured image field and the fiber mode must be wider than the spatial Fourier profile of the plane wave decomposition component so that the probe measurement accurately reflects the correct field distribution. Since the NSOM probe's aperture diameter is small, this condition is satisfied.

Experimental results

Figure 20b shows the focal spot with the vortex phase plate removed. The spot symmetric, with a spot size of 600 nm and a central intensity maximum. A line plot of the intensity is also given. The calculated profile is shown in the graph on the far right. The calculate spot size using the Airy formula [84] for point source with 0.85 NA objective gives a spot size of 380 nm. The larger spot size (600 nm) is due to the Gaussian lateral intensity of the collimated beam at the back of the focal plane of the objective, which decreases the beam width compared to a plane wave.

The back transmission throughput of the probe determines the coupling efficiency from the tip to the fiber input end of photons overlapping the NSOM tip aperture. The detected signal is low for aperture diameters below the diffraction limit. Since increasing focus power will cause excess heating, the power must be kept low to prevent melting the gold coating on the NSOM fiber tip [85].

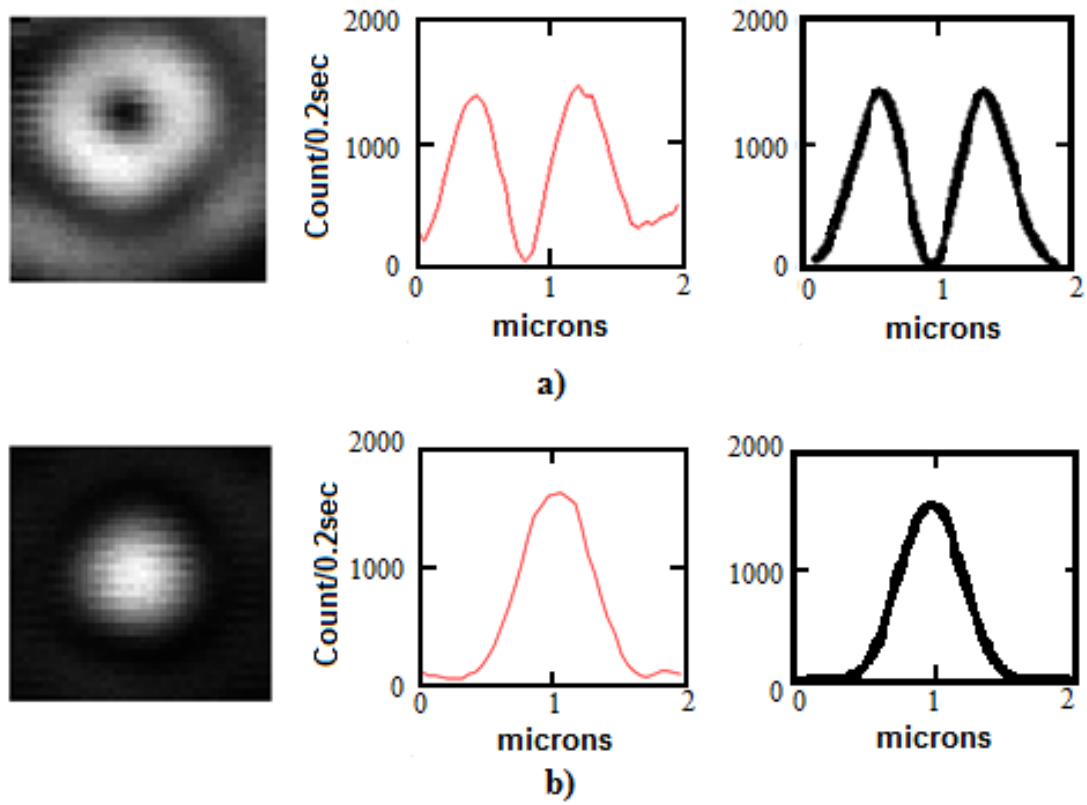

Figure 20. (a) Image of a 2x2 μm scan of the focal spot of the depletion beam using an objective with NA=0.85. The measured and calculated intensity plots through the central region are also given on the center and far right. (b) Image of the focal spot with the VPP removed. Number of pixels is 1600. The integration time for each pixel is 0.2 seconds. The calculated result is also shown. Reproduced with permission of IOP Publishing.

The photon count rate detected by the PMT is $\eta \cdot \frac{\kappa \cdot \beta \cdot P}{h\nu}$. η is the quantum efficiency of the PMT. β is the fraction of the focused light which overlaps the aperture of the NSOM probe tip. P is power of the focused light. hυ is the photon energy. κ is the throughput of light into the NSOM probe's aperture. The PMT's efficiency at 628 nm is

rated as η= 0.0036. β is determined by calculating the number of photons within the 100 nm aperture using the data from Figure 3b, which gives β=0.028. With P=0.2 mW and peak photon count of 1600 photons per 0.2 second, the back transmission throughput κ is approximately 10^{-7}. Note that the transmission throughput of a NSOM probe (from fiber input end to tip) is approximately 10^{-5}-10^{-6} [24].

Summary

Super-resolution fluorescent microscopy and activation-deactivation photolithography require that the focal spot of the doughnut shape depletion beam be precisely known. It was shown that a NSOM fiber probe can be effective for imaging the depletion beam's focal spot. Calculation of the doughnut shape focal spot agrees well with the measured results. NSOM probes offer superior repeatability and control, compared to using a gold nanoparticle or fluorescent bead.

6. STED MICROSCOPY FOR THE CASE WHEN BOTH THE EXCITATION AND THE DEPLETION BEAM PASS THROUGH A COMMON VORTEX PHASE PLATE

Overview

As described in previous chapter, the traditional method of STED microscopy is to allow only the depletion beam to pass through the vortex phase plate. The excitation focal spot is Gaussian in shape and the depletion focal spot is a donut shape. In this chapter STED performance is calculated when both the excitation and depletion beams pass through a common vortex phase plate. As expected both the excitation and depletion focal spots now exhibit a donut shape. However, it is found that the two donut focal spots are displaced from each other by about 70 nm. Calculations show that for achieving the same lateral super-resolution, the required depletion power is now reduced by a factor of almost ten with modest trade-off in terms of fluorescent signal level. The reason for this improvement is that the depletion effect is more efficient as will be discussed below.

Optical setup

The STED microscope design used in this work is described here. The transmission-reflection spectral characteristics of the optical components used in the design are chosen based on the absorption and emission spectra of the particular dye used. The optical filter components are chosen for imaging Invitrogen F8800 100 nm diameter orange fluorescent beads and ATTO 532 dyes.

The STED microscope is shown in Figure 21. A low NA objective is used to collimate the light from one end of an optical fiber, the other end is the input light from the

supercontinuum white light source. A dichroic beamsplitter splits the beam. Light with a wavelength longer than 532 nm is transmitted through the dichroic beamsplitter, and a band of short wavelength light below 532 nm is reflected. The light that is transmitted through the dichroic filter is filtered by a bandpass filter centered at 607 nm with a pass-band width of 36 nm. The shorter wavelength light is filtered by a 475/50 nm bandpass filter. A second dichroic beam splitter combines the shorter and longer wavelength light. A low NA (0.2) microscope objective is used to focus the light into a single mode fiber.

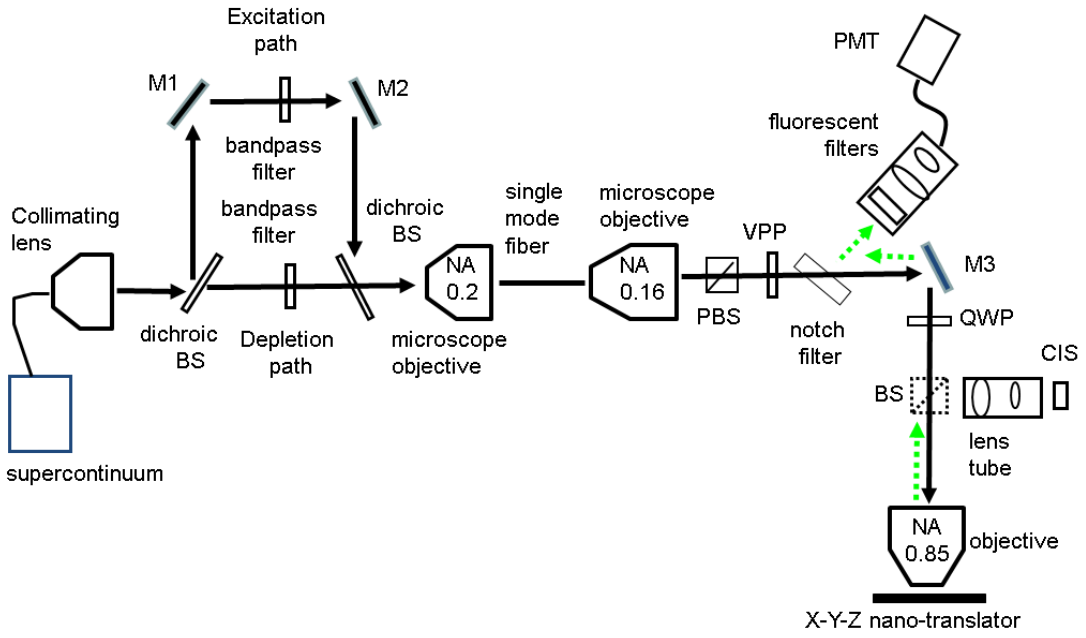

Figure 21. Design of the STED microscope. PBS: polarization beam splitter. M: mirror. BS: beam splitter. VPP: vortex phase plate. QWP: quarter wave plate. PMT: photomultiplier. CIS: CMOS image sensor.

A low NA (0.16) microscope objective collimates the light that is output from the single mode fiber. The light is first polarized by a polarization beam splitter (PBS). Polarized light is needed so that it can be used in conjunction with the vortex phase plate and the quarter-wave plate to produce a focal spot with a central dark region. The vortex phase plate (VPP) and the subsequent quarter-wave plate shape the beam that, upon focusing by the apochromatic microscope objective with high numerical aperture (0.85), the beam cross-section exhibits a doughnut shape central dark region appropriate for achieving lateral super resolution. Both the excitation and depletion beams pass through the VPP and quarter wave plate. Because the excitation and depletion beams exit from a common single mode fiber, both beams are collinear.

The excitation and depletion beams are reflected downward by a mirror and then focused onto the sample by a microscope objective which is mounted on the rotating turret of the Olympus model MX 50A-F microscope frame. Fluorescent signal collected by the high NA microscope objective propagates backward. Its path is shown by the dashed line. The fluorescent light from the sample retraced the original transmission path to the notch filter at which point it is reflected into the lens tube and then focused into a multimode fiber. A PMT is used to measure the fluorescent count. The 563/9 bandpass filter (not shown) is placed inside the lens tube unit.

A beam splitter (BS) is placed before the high NA objective and is used in conjunction with the lens tube and the CMOS image sensor to view the sample and monitor the focal spot. The components used in the optical setup are summarized in Table 3.

Table 3. Components used in the optical setup

Components	**Make**	**Model number**
Supercontinuum light source	Koheras	SuperK compact
apochromatic objective	Olympus	UPLSApo 4x/0.16
Apochromatic objective	Olympus	UPlanx40 0.85 NA
notch filters	Semrock	FF03-561/13
dichroic beamsplitter	Semrock	Di01-R532
bandpass filters	Semrock	FF01-607/36
bandpass filters	Semrock	FF01-475/50
vortex phase plate	RPC Photonics	VPP-1
achromatic quarter waveplate	Thorlabs	AQWP05M
broadband dielectric mirrors	Thorlabs	BB1-E02
precision kinematic mirror mount	Thorlabs	KS2D
nano-translators	Melles Griot/Thorlabs	Max603D

Electric field calculation using vectorial representation

Most of the equations needed for the calculation are described in chapter 3. One modification is the function $F_\phi(\phi)$ for the vortex phase plate:

$$F_\phi(\phi) = \exp\left(i \cdot \phi \cdot \gamma\right) \tag{17}$$

We choose the plate such that the spiral is of charge 1 at the depletion wavelength of 607 nm. Thus, γ=1 for 607 nm wavelength. However, for the excitation wavelength of 475 nm,

γ = 607/475. With this modification the predicted donut shape excitation and depletion focal is spatially shifted by about 70 nm with respect to each other, which will be validated by the measurement result shown below.

Rate equations for describing the depletion effects

As pointed out in the previous chapter dye molecule energy states generally consist of both singlet and triplet states. So, exact rate equation description is not realistic. However, if we assume that the experimental bleaching effect is such that it is minor, then we should be able to predict approximately the depletion effect by a simple rate equation analysis by neglecting the transition into the triplet state. Thus, we take an absorption cross-section σ_{12} and a emission cross-section σ_{21}, and assume that the excited states and the ground states molecular density consist of the sum of all the states in its two manifold. Then, the rate equation describing the excited state population N_2 is given by,

$$\frac{dN_2(r,t)}{dt} = \left[\sigma_{12} \cdot \frac{P_e(r,t)}{h\upsilon_e}\right] \cdot N_1(r,t) - \left[\sigma_{21} \cdot \frac{P_D(r,t)}{h\upsilon_D} + \frac{1}{\tau}\right] \cdot N_2(r,t) \tag{18}$$

$$N_1 = N - N_2 \tag{19}$$

N_1 is the ground state population, and N is the total molecular density. λ_e and λ_D are the excitation and depletion wavelengths, respectively. Their corresponding frequencies are υ_e and υ_D. τ is the recombination lifetime. P_e is the excitation power per area, and P_D is the depletion power per area. Excitation and depletion power are both time-dependent because the laser is pulsed with a pulse width of 2 ns. The emission cross-section σ_{21} is taken as $1\text{x}10^{-16}$ cm^2 and the absorption cross section σ_{12} is taken as $2.7\text{x}10^{-17}$ cm^2 as given in reference [86] for ATTO 532 dyes. To reduce computation time, the laser pulse

is assumed to be a square wave in time. Then, by time integration of the rate equation, N_2 can be written as,

$$N_2 = \frac{\sigma_{12} \cdot \frac{P_e}{h\upsilon_e} \cdot N \cdot \left[1 - \exp\left[-\left(\sigma_{21} \cdot \frac{P_D}{h\upsilon_D} + \sigma_{12} \cdot \frac{P_e}{h\upsilon_e} + \frac{1}{\tau}\right)\right]\right] \cdot w}{\sigma_{21} \cdot \frac{P_D}{h\upsilon_D} + \sigma_{12} \cdot \frac{P_e}{h\upsilon_e} + \frac{1}{\tau}} \tag{20}$$

Here, w is the pulse width of the laser, which is 2 ns.

The fluorescent power P_{spon}, with units of power per volume per wavelength, is described by,

$$P_{spon} = \frac{8\pi \cdot n^2 \cdot c}{\lambda^4} \cdot \sigma_{21} \cdot N_2 \tag{21}$$

Results

Numerical simulations were performed by calculating the optical field at the focal plane using MathCad codes in combination with the rate equation. For the simulations, the wavelengths of light chosen were based upon the excitation and depletion spectra of Invitrogen F8800 100 nm diameter orange fluorescent beads, which is very similar with the ATTO 532 dyes. The measured spatial profile of the donut and the Gaussian focal spots (without the vortex phase plate) at the focal plane was measured by NSOM as discussed in the previous chapters. It was shown that the calculated profiles agree very well with measured results. Here we presented more data on the donut shape profile as measure by the CMOS camera after magnification by the lens tube. The right column of Figure 22 shows the focal spot recorded using the CMOS camera for the excitation and the depletion beams. The bottom most figure shows the focal spot of the excitation beam when the phase

plate is change to one with charge equal one at the wavelength of 808 nm (γ =808/475).

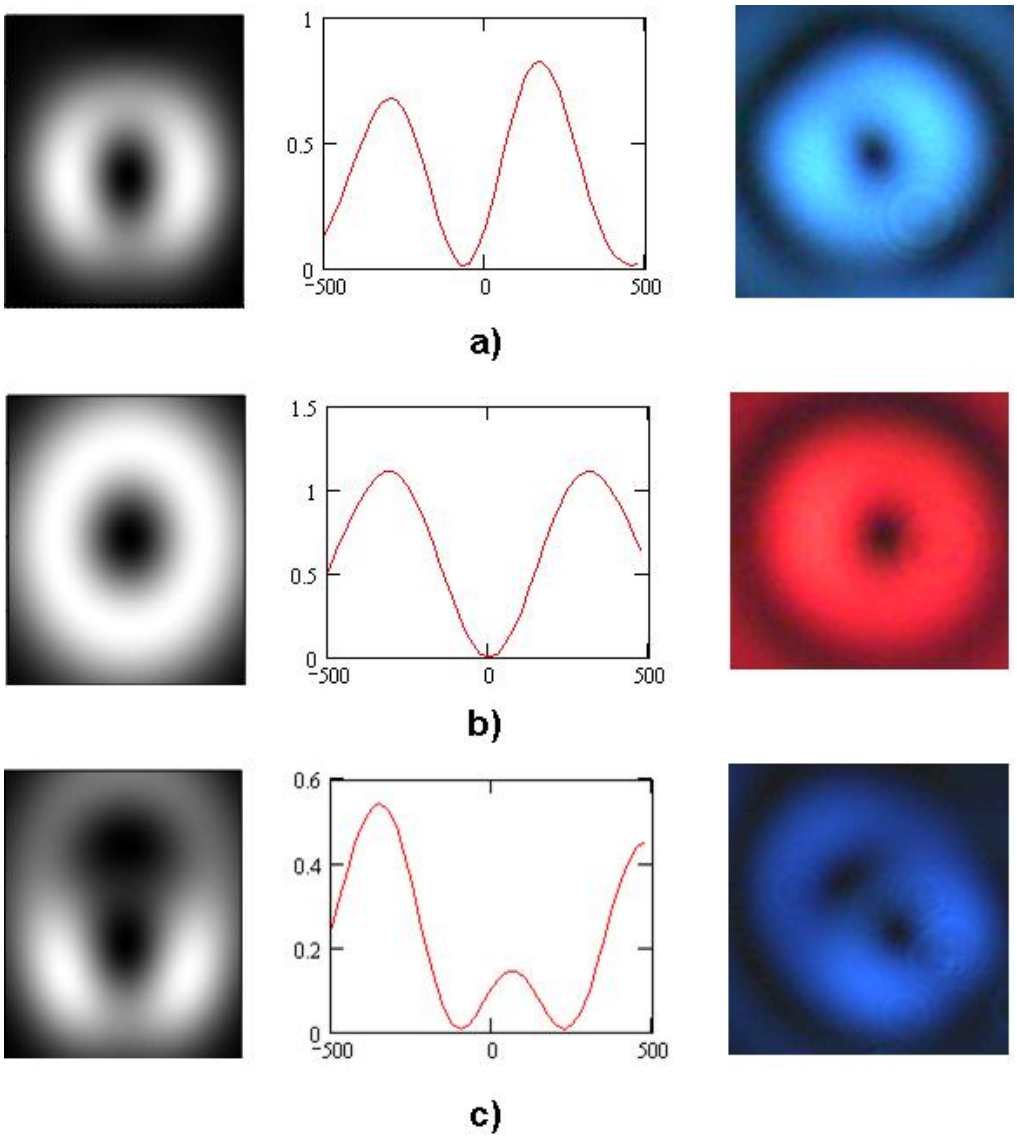

Figure 22. Electric field intensity in the focal plane. The left and center column are the calculated results. The right column are the measured results using the CMOS camera. a) λ = 475 nm, b) λ = 607 nm, and c) λ = 475 nm with 808 nm vortex phase plate.

To more clearly show the relative displacement of the excitation and the depletion focal spots, we have both 475 nm and 607 nm light simultaneously passing through the vortex phase plate. The two measured focal spots are displayed simultaneously and the intensity display on the CMOS camera are deliberately saturated to better reveal the two shifted central intensity minimum because the blue light will fill the red void and the red light will fill the blue void, as shown in Figure 23. There is a lateral shift between the optical vortices for the 475 nm and 607 nm spots, and the shift is roughly about 70 nm as predicted by calculations.

Note that measuring the lateral shift using the CMOS image sensor gives a value of 130 nm. This value includes the shift due to the vortex phase plate and the shift due to the dispersion of the optical components along the beam path. The shift due the optical components can be corrected by moving the phase plate to the region where there is no vortex function. The shift due solely to the optical was measured to be 60 nm. From the numerical simulation results, the lateral shift is 75 nm apart. So, accounting for the additional shift due to the optical components gives the correct shift of about 75 nm. In conclusion, we show that there is very good agreement between simulation results and experimental results with regards to the spatial profile of the excitation and depletion focal spots. Therefore, the vectorial representation of the electric field closely matches the experimental results obtained using our STED microscope.

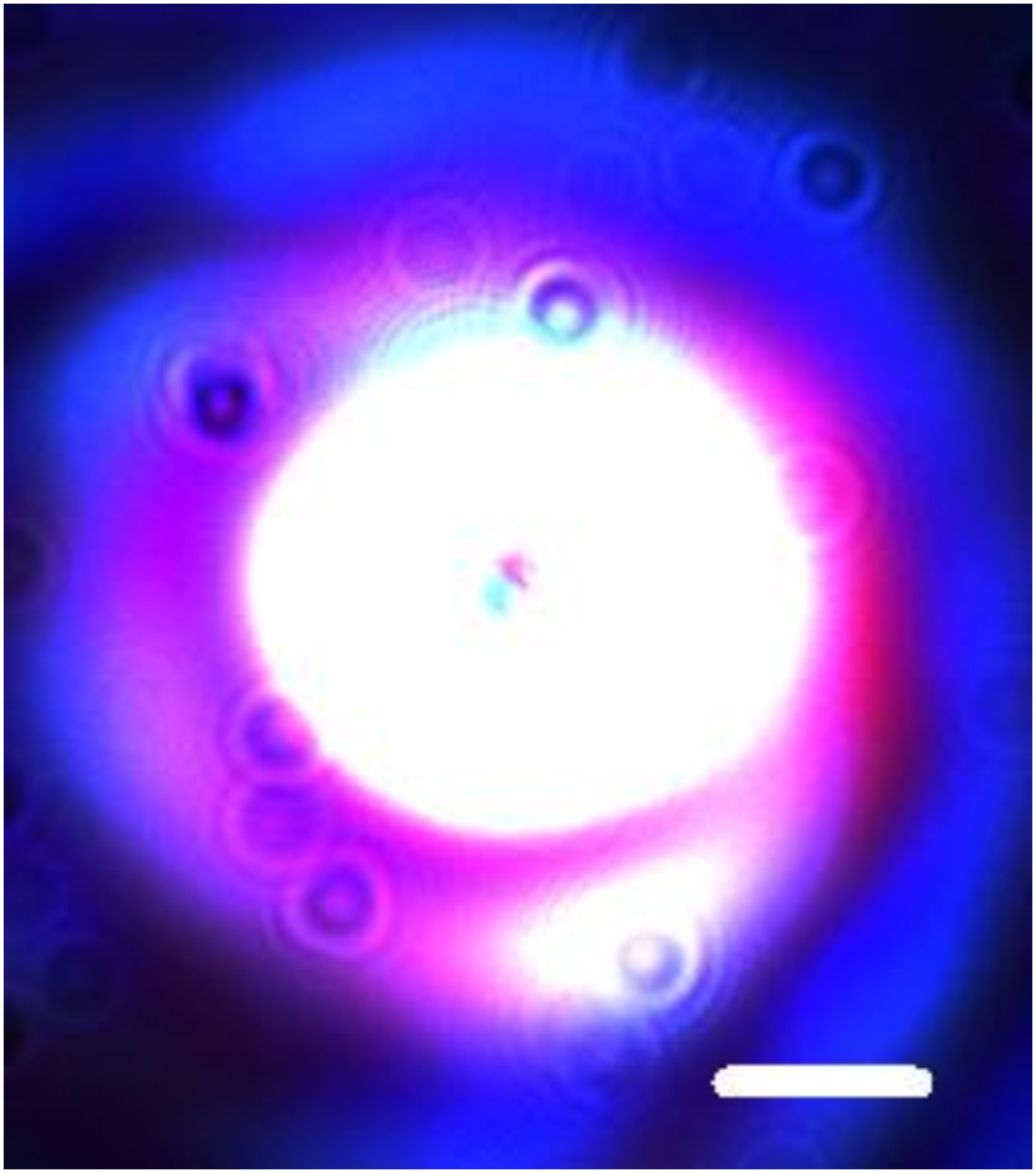

Figure 23. Electric field intensity in the focal plane of the donut shaped excitation and depletion spots with both wavelengths (475 nm and 607 nm) pass through the vortex phase plate. The shift is about 130 nm as shown. Scale bar is 1 μm.

Resolution comparison

Using vectorial representation of the electric field and the rate equations, the resolution of the proposed STED microscope, with excitation and depletion beams using a common vortex phase plate, is compared to the resolution obtained via conventional STED microscope. For conventional STED microscope, the excitation beam is Gaussian, and the depletion beam has a central intensity null. For the proposed STED microscope in these simulations, λ = 475 nm for excitation and λ=607 nm for the depletion beam, and the vortex phase plate as a charge of 1 at 607 nm.

Figure 24a shows depletion power versus resolution. For the proposed STED microscope, the resolution is improved by approximately 2.3 times for the same depletion power and about 5 times less depletion power for the same resolution compared to conventional STED.

Figure 24b shows fluorescent counts versus resolution. For the proposed STED microscope, the fluorescent counts are reduced by approximately 20%, compared to conventional STED.

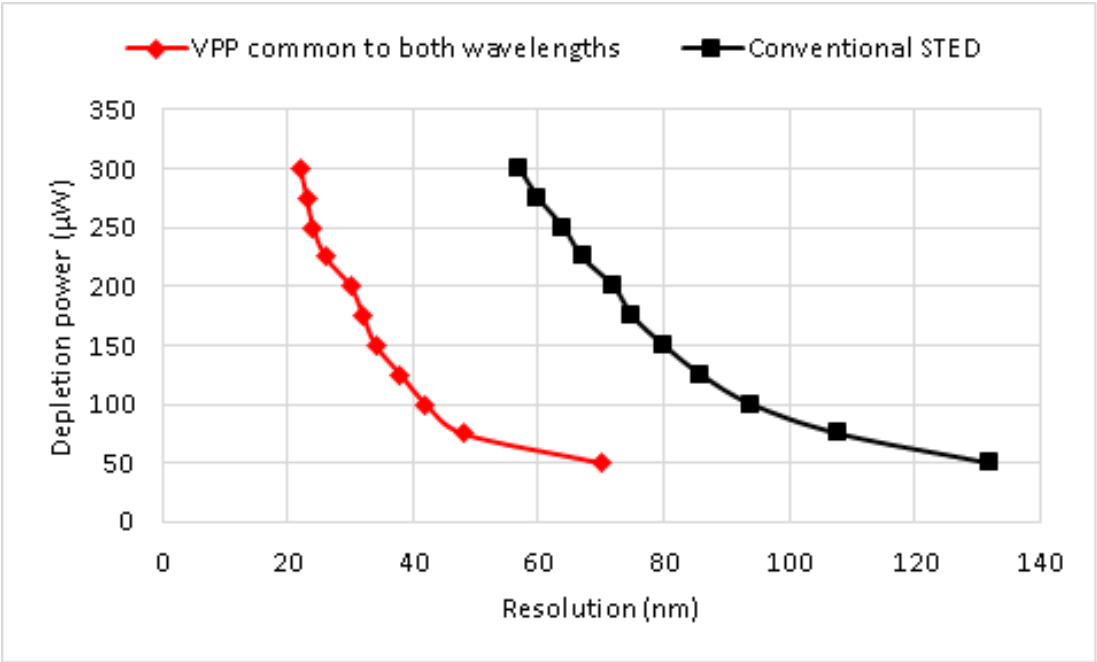

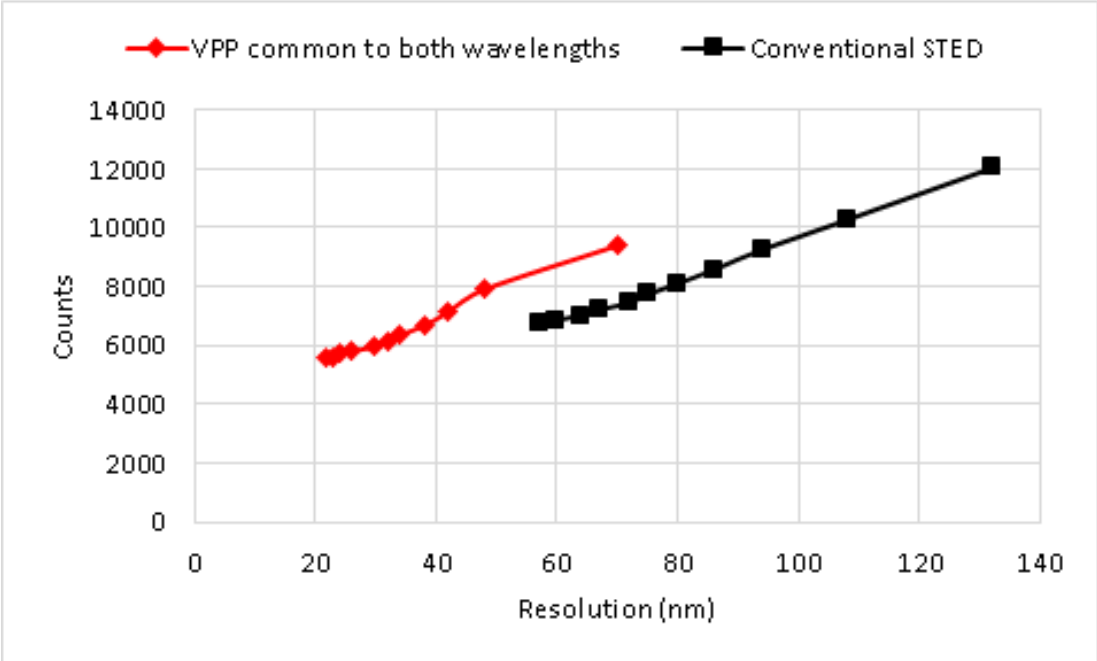

Figure 24. Comparison of conventional STED microscope and the proposed STED microscope using VPP common to both excitation and depletion beams. a) depletion power versus resolution, b) fluorescent counts versus resolution.

Summary

In this chapter STED performance was calculated when both the excitation and depletion beams pass through a common vortex phase plate. As expected both the excitation and depletion focal spots now exhibited a donut shape. However, it was found that the two donut focal spots were displaced from each other by about 70 nm. Calculations show that for achieving the same lateral super-resolution, the required depletion power is now reduced by a factor of almost ten with modest trade-off in terms of fluorescent signal level. The reason for this improvement was that the depletion effect was more efficient.

7. CONCLUSIONS AND FUTURE WORK

Conclusions

NSOM probes are useful for obtaining sub-diffraction images of surfaces. However, NSOM probes will melt when the input laser power is too large. So, the input laser power must be very small to avoid damaging the NSOM probe. This causes the scan time to be very long, and NSOM probes are impractical for applications which require very high laser power.

To overcome the problems associated with NSOM probe heating, NSOM probes with epoxy heat sinks were fabricated. The position of controlled so that the probe's aperture protruded out of the epoxy by only 2-3 microns. SEM, EDS, and BSE were used to examine the NSOM probes to verify the integrity of the epoxied NSOM probes. Optical imaging and optical power measurements verified that the NSOM probe was not damaged when 405 nm light, at an input power of 21.4 mW, was coupled into the NSOM probe.

NSOL using a NSOM probe with epoxy heat sinks was demonstrated. The input optical power was increased to 20 mW (cw-laser, λ = 400 nm) without damaging the NSOM probe. The probe was used to expose though 93 nm thick photoresist at 62 μs dwell time, giving a potential line scan of about 300 μm/sec with a 100 nm NSOM probe.

In the second part of this study, a versatile STED fluorescent microscope, with a configuration appropriate for using excitation and depletion beams from any supercontinuum light source, was de-scribed. The versatility of the microscope allows this microscope to be used with a variety of different fluorescent dyes because only the optical filters need

to be changed. The components of the microscope were placed on standard microscope frame. The collinear depletion and excitation beams were focused by a 0.9 NA microscope objective, producing a 90 nm de-convoluted lateral super-resolution, which was verified by imaging 100 nm diameter beads.

Super-resolution fluorescent microscopy requires that the focal spot of the dough-nut shape de-pletion beam be precisely known. It was shown that a NSOM fiber probe can be effective for imaging the depletion beam's focal spot. Calculation of the doughnut shape focal spot agrees well with the measured results. NSOM probes offer superior re-peatability and control, compared to using a gold na-noparticle or a fluorescent bead. Conventional STED microscopes use a donut shaped depletion beam and Gaussian exci-tation beam. The performance of a STED microscope was calculated when both the exci-tation and depletion beams pass through a common vortex phase plate. As expected both the excitation and depletion focal spots now exhibited a donut shape. However, it was found that the two donut focal spots were dis-placed from each other by about 70 nm.

Calculations were performed to compare the performance of a conventional STED microscope to a STED microscope which uses a common vortex phase plate for both the excitation and depletion beams. Calculations showed that for achieving the same lateral su-per-resolution, the required depletion power was now reduced by a factor of almost ten with modest trade-off in terms of fluorescent signal level. The reason for this improvement was that the depletion effect was more efficient.

Future work

The current study can be extended for the investigation three dimensional cellular features. It was concluded from this research that lateral super resolution can be achieved using a common vortex phase plate for the excitation and depletion beams. This study can be extended to modify the design of the STED microscope so that axial super resolution is also achieved. To achieve axial super resolution, the following factors should be studied in the future.

i. Effect of a step phase plate on the excitation and depletion beams.
ii. Effect of astigmatism on the excitation and depletion beams.
iii. Effect of defocusing on the excitation and depletion beams.

REFERENCES

[1] U. Dürig, D. Pohl, and F. Rohner, "Near-field optical scanning microscopy," *Journal Applied Physics,* vol. 59, 3318 (1986).

[2] Y. Oshikane, T. Kataoka, M. Okuda, S. Hara, H. Inoue, and M. Nakano, "Observation of nanostructure by scanning near-field optical microscope with small sphere probe," *Science and Technology of Advanced Materials,* vol. 8, pp. 181-185 (2007).

[3] V. Sandoghdar, J. Michaelis, C. Hettich, and J. Mlynek, "Optical microscopy using a single-molecule light source," *Nature,* vol. 405, pp. 325-328 (2000).

[4] A. Lewis, M. Isaacson, A. Harootunian, and A. Murray, "Development of a 500 Å spatial resolution light microscope. I. Light is efficiently transmitted through λ/16 diameter apertures," *Ultramicroscopy,* vol. 13, pp. 227-231 (1984).

[5] A. Larosa, B. Yakobson, and H. Hallen, "Origins and effects of thermal-processes on near-field optical probes," *Applied Physics Letters,* vol. 67, pp. 2597-2599 (1995).

[6] P. Gucciardi, M. Colocci, M. Labardi, and M. Allegrini, "Thermal-expansion effects in near-field optical microscopy fiber probes induced by laser light absorption," *Applied Physics Letters,* vol. 75, pp. 3408-3410 (1999).

[7] C. Lienau, A. Richter, and T. Elsaesser, "Light-induced expansion of fiber tips in near-field scanning optical microscopy," *Applied Physics Letters,* vol. 69, pp. 325-327 (1996).

[8] B. Yakobson, A. LaRosa, H. Hallen, and M. Paesler, "Thermal/optical effects in NSOM probes," *Ultramicroscopy*, vol. 61, pp. 179-185 (1995).

[9] C. Cremer and T. Cremer, "Considerations on a laser-scanning-microscope with high resolution and depth of field," *Microscopica Acta*, vol. 81, pp. 31–44 (1978).

[10] V. Westphal, S. Rizzoli, M. Lauterbach, D. Kamin, R. Jahn, and S. Hell, "Video-rate far-field optical nanoscopy dissects synaptic vesicle movement," *Science*, vol. 320, pp. 246–249 (2008).

[11] S. Hell and J. Wichmann, "Breaking the diffraction resolution limit by stimulated emission: stimulated-emission-depletion fluorescence microscopy," *Optics Letters*, vol. 19, pp. 780–782 (1994).

[12] T. Klar and S. Hell, "Subdiffraction resolution in far-field fluorescence microscopy," *Optics Letters*, vol. 24, pp. 954–956 (1999).

[13] S. Hess, T. Giriajan, and M. Mason, "Ultra-high resolution imaging by fluorescence photoactivation localization microscopy," *Biophysical Journal*, vol. 91, pp. 4258–4272 (2006).

[14] T. Müller, C. Schumann, and A. Kraegeloh, "STED microscopy and its applications: new insights into cellular processes on the nanoscale," *ChemPhysChem*, vol. 13, pp. 1986–2000 (2012).

[15] M. Dyba and S. Hell, "Photostability of a fluorescent marker under pulsed excited-state depletion through stimulated emission," *Applied Optics*, vol. 42, pp. 5123–5129 (2003).

[16] P. Török and P. Munro, "The use of Gauss-Laguerre vector beams in STED

microscopy," *Optics Express*, vol. 12, pp. 3605–3617 (2004).

[17] J. Keller, A. Schönle, and S. Hell, "Efficient fluorescence inhibition patterns for RESOLFT microscopy," *Optics Express*, vol. 15, pp. 3361–3371 (2007).

[18] S. Hell and M. Reuss, "Birefringent device converts a standard scanning microscope into a STED microscope that also maps molecular orientation," *Optics Express*, vol. 18, pp. 1049–58 (2010).

[19] D. Wildanger, B. Patton, H. Schill, L. Marseglia, J. Hadden, S. Knauer, A. Schönle, J. Rarity, J. O'Brien, S. Hell, and J. Smith, "Solid immersion facilitates fluorescence microscopy with nanometer resolution and sub- ångström emitter localization," *Advanced Materials*, vol. 24, pp. 309-313 (2012).

[20] A. Tseng, "Recent developments in nanofabrication using scanning near-field optical microscope lithography," *Optics & Laser Technology*, vol. 39, pp. 514-526 (2007).

[21] C. Bouwkamp, "Diffraction theory," *Philips Research Reports*, vol. 5, pp. 321-332 (1950)

[22] H. Bethe, "Theory of diffraction by small holes," *Physical Review*, vol. 66, pp. 163-182 (1944).

[23] D. Labeke, D. Barchiesi, and F. Baida, "Optical characterization of nanosources used in scanning near-field optical microscopy," *Journal Optical Society of America A*, vol. 12, pp. 695-703 (1995).

[24] S. Juodkazis, Y. Arisawa, S. Matsuo, H. Misawa, R. Tomasiunas, and J. Vaitkus, "Submicrometer lithography by near-field optical microscopy," *Proceedings of*

SPIE, vol. 4318, pp. 42-47 (2001).

[25] R. Stockle, N. Schaller, V. Deckert, C. Fokas, and R. Zenebi, "Brighter near-field optical probes by means of improving the optical destruction threshold," *Journal of Microscopy*, vol. 194, pp. 378-382 (1999).

[26] L. Novotny, and B. Hecht, "Principle of nano-optics," *Cambridge University Press*, pp. 184. (2006)

[27] A. Soni, and S. Wen, "Non-intrusive temperature measurement of NSOM probes with thermoreflectance imaging," *Journal of Physics D: Applied Physics*, vol. 45, pp. 1-8 (2012).

[28] M. Stahelin, M. Bopp, G. Tarrach, A. Meixner, and I. Zschokke-Granacher, "Temperature profile of fiber tips used in scanning near-field optical microscopy," *Applied Physics Letters*, vol. 68, pp. 2603-2605 (1996).

[29] P. Gucciardi, M. Colocci, M. Labardi, and M. Allegrini, "Thermal-expansion effects in near-field optical microscopy fiber probes induced by laser light absorption," *Applied Physics Letters*, vol. 75, pp. 3408-3410 (1999).

[30] C. Lienau, A. Richter, and T. Elsaesser, "Light-induced expansion of fiber tips in near-field scanning optical microscopy," *Applied Physics Letters*, vol. 69, pp. 325-327 (1996).

[31] A. Rosa, B. Yakobson, and H. Hallen, "Origins and effects of thermal processes on near-field optical probes," *Applied Physics Letters*, vol. 67, pp. 2597-2599 (1995).

[32] L. Thiery, N. Marini, J. Prenel, M. Spajer, C. Bainier, and D. Courjon,

"Temperature profile measurements of near-field optical microscopy fiber tips by means of sub-micronic thermocouple," *International Journal of Thermal Sciences,* vol. 39, pp. 519-525 (2000).

[33] H. Janseny, H. Gardeniers, M. de Boer, M. Elwenspoek, and J. Fluitman, "A survey on the reactive ion etching of silicon in microtechnology," *Journal of Micromechanics and Microengineering*, vol. 6, pp. 14–28 (1996).

[34] D. Labeke, D. Barchiesi, and F. Baida, "Optical characterization of nanosources used in scanning near-field optical microscopy," *Journal of the Optical Society of America A*, vol. 12, pp. 695-703 (1995).

[35] Y. Lin, M. Hong, W. Wang, T. Law and T. Chong, "Lithography in UV photoresist using NSOM," *Proceedings of SPIE,* vol. 5662, pp. 77-82 (2004).

[36] R. Riehn, A. Charas, J. Morgado, and F. Cacialli, "Near-field optical lithography of a conjugated polymer," *Applied Physics Letters*, vol. 82, pp. 526-528 (2003).

[37] S. Takahashi, K. Samata, H. Muta, S. Machida, and K. Horie, "Refractive-index patterning using near-field scanning optical microscopy," *Applied Physics Letters*, vol. 78, pp. 13-15 (2001).

[38] V. Likodimos, M. Labardi, L. Pardi, M. Allegrini, and M. Giordano, "Optical nanowriting on azobenzene side-chain polymethacrylate thin films by near-field scanning optical microscopy," *Applied Physics Letters,* vol. 82, pp. 3313-3315 (2003).

[39] A. Naber, H. Kock, and H. Fuchs, "High-resolution lithography with near-field optical microscopy," *Scanning*, vol. 18, pp. 567-571 (1996).

[40] U. Durig, D. Pohl, and F. Rohner, "Near-field optical-scanning microscopy," *Journal of Applied Physics,* vol. 59, pp. 3318-3327 (1986).

[41] A. Harootunian, E. Betzig, M. Isaacson, and A. Lewis, "Super-resolution fluorescence near-field scanning optical microscopy," *Applied Physics Letters,* vol. 49, pp. 674-676 (1986).

[42] A. Kramer, T. Hartmann, R. Eschrich, and R. Guckenberger, "Scanning near-field fluorescence of thin organic films at the water/air interface," *Ultramicroscopy,* vol. 71, pp. 123-132 (1998).

[43] J. Hsu, M. Lee, and B. Deaver, "A nonoptical tip–sample distance control method for near-field scanning optical microscopy using impedance changes in an electromechanical system," *Review of Scientific Instruments,* vol. 66, pp. 3177-3181 (1995).

[44] A. Kramer, T. Hartmann, S. Stradler, and R. Guckenberger, "An optical tip-sample distance control for a scanning optical microscope," *Ultramicroscopy,* vol. 62, pp. 191-195 (1995).

[45] Y. Lin, M. Hong, W. Wang, Y. Law, and T. Chong, "Sub-30 nm lithography with near-field scanning optical microscope combined with femtosecond laser," *Applied Physics A,* vol. 80, pp. 461-465 (2005).

[46] S. Hell and J. Wichmann, "Breaking the diffraction resolution limit by stimulated emission: stimulated-emission-depletion fluorescence microscopy," *Optics Letters,* vol. 19, pp. 780-782 (1994).

[47] B. Hein, K. Willig, and S. Hell, "Stimulated emission depletion (STED) nanoscopy

of a fluorescent protein-labeled organelle inside a living cell," *Proceedings of the National Academy of Sciences*, vol. 105, pp. 14271-14726 (2008).

[48] R. Schmidt, C. Wurm, S. Jakobs, J. Engelhardt, A. Egner, and S. Hell, "Spherical nanosized focal spot unravels the interior of cells," *Nature Method*, vol. 5, pp. 539-544 (2008)

[49] M. Reuss, J. Engelhardt, and S. Hell, "Birefringent device converts a standard scanning microscope into a STED microscope that also maps molecular orientation," *Optics Express*, vol. 18, pp. 1049-1058 (2010).

[50] R. Heintzmann, T. Jovin, and C. Cremer, "Saturated pattern excitation microscopy- a concept for optical resolution improvement," *Journal of the Optical Society of America A*, vol. 19, pp. 1599-1609 (2002).

[51] M. Gustafsson, "Nonlinear structured-illumination microscopy: Wide field fluorescence imaging with theoretically unlimited resolution," *Proceedings of the National Academy of Sciences*, vol. 102, pp. 13081-13086 (2005).

[52] S. Hess, T. Girirajan, and M. Mason, "Ultra-high resolution imaging by fluorescence photoactivation localization microscopy," *Biophysical Journal*, vol. 91, pp. 4258-4272 (2006).

[53] E. Betzig, G. Patterson, R. Sougrat, O. Lindwasser, S. Olenych, J. Bonifacino, M. Davidson, J. Lippincott-Schwartz, and H. Hess, "Imaging intracellular fluorescent proteins at nanometer resolution," *Science*, vol. 313, pp. 1642-1645 (2006).

[54] M. Rust, M. Bates, and X. Zhuang, "Sub-diffraction-limit imaging by stochastic optical reconstruction microscopy (STORM)," *Nature Methods*, vol. 3, pp. 793-

796 (2006).

[55] M. Bates, B. Huang, G. Dempsey, and X. Zhuang, "Multicolor super-resolution imaging with photo-switchable fluorescent probes," *Science,* vol. 317, pp. 1749-1753 (2007).

[56] B. Huang, W. Wang, M. Bates, and X. Zhuang, "Three-dimensional super-resolution imaging by stochastic optical reconstruction microscopy," *Science,* vol. 319, pp. 810-813 (2008).

[57] N. Heckenberg, R. McDuff, C. Smith, and A. White, "Generation of optical phase singularities by computer-generated holograms," *Optics Letters,* vol. 17, pp. 221-223 (1992).

[58] B. Richards and E. Wolf, "Electromagnetic diffraction in optical systems II. Structure of the image field in a aplanatic system," *Proceedings of the Royal Society of London. Series A. Mathematical and Physical Sciences,* vol. 253, pp. 358-379 (1959).

[59] D. Wildanger, R. Medda, L. Kastrup, and S. Hell, "A compact STED microscope providing 3D nanoscale resolution," *Journal of Microscopy,* vol. 236, pp. 35-43 (2009).

[60] Y. Iketaki, T. Watanabe, N. Bokor, and M. Fujii, "Investigation of the center intensity of first- and second-order Laguerre-Gaussian beams with linear and circular polarization," *Optics Letters,* vol. 32, pp. 2357-2359 (2007).

[61] V. Westphal and S. Hell, "Nanoscale resolution in the focal plane of an optical microscope," *Physical Review Letters,* vol. 94, pp. 1-4 (2005).

[62] K. Murooka, K. Hattori, and O. Iizuka, “Initial results of a 50 kV electron beam writer EBM-4000 for a 90 nm node photomask,” *Journal Vacuum Science & Technology B*, vol. 21, pp. 2668-26671 (2003).

[63] J. Fourkas, “Nanoscale photolithography with visible light,” *Journal of Physical Chemistry Letters*, vol. 1, pp. 1221-1227 (2010).

[64] L. Li, R. Gattass, E. Gershgoren, H. Hwang, and J. Fourkas, “Achieving λ/20 resolution by one-color initiation and deactivation of polymerization,” *Science*, vol. 324, pp. 910-913 (2009).

[65] T. Scott, B. Kowalski, A. Sullivan, C. Bowman, and R. McLeod, “Two-color single-photon photoinitiation and photoinhibition for subdiffraction photolithography,” *Science*, vol. 324, 913-917 (2009).

[66] J. Fischer, G. von Freymann, and M.Wegener, “The materials challenge in diffraction-unlimited direct-laser-writing optical lithography,” *Advanced Materials*, vol. 22, pp. 3578-3582 (2010).

[67] Y. Zongsong, R. Evans, and M. Gu, 2013, “Three-dimensional deep sub-diffraction optical beam lithography with 9 nm feature size,” *Nature Communications*, vol. 4, pp. 1-7 (2013).

[68] T. Andrew, H. Tsai, and R. Menon, “Confining light to deep subwavelength dimensions to enable optical nanopatterning,” *Science*, vol. 324, pp. 917-921 (2009).

[69] R. Menon and H. Smith, “Absorbance-modulation optical lithography,” *Journal of the Optical Society of America A*, vol. 23, pp. 2290-2294 (2006).

[70] R. Menon, H. Tsai, and S. Thomas, "Far-field generation of localized light fields using absorbance modulation," *Physical Review Letters,* vol. 98, pp. 1-4 (2007).

[71] H. Tsai, G. Walraff, and R. Menon, "Spatial-frequency multiplication via absorbance modulation," *Applied Physics Letters,* vol. 91, pp. 1-3 (2007).

[72] N. Brimhall, T. Andrew, R. Manthena, and R. Menon, "Breaking the far-field diffraction limit in optical nanopatterning via repeated photochemical and electrochemical transitions in photochromic molecules," *Physical Review Letters,* vol. 107, pp. 1-5 (2011).

[73] R. Schmidt, C. Wurm, S. Jakobs, J. Engelhardt, A. Egner, and S. Hell, "Spherical nanosized focal spot unravels the interior of cells," *Nature Methods,* vol. 5, pp. 539-544 (2008).

[74] Y. Iketaki, T. Watanabe, N. Bokor, and M. Fujii, "Investigation of the center intensity of first- and second-order Laguerre-Gaussian beams with linear and circular polarization," *Optics Letters,* vol. 32, pp. 2357-2359 (2007).

[75] V. Westphal and S. Hell, "Nanoscale resolution in the focal plane of an optical microscope," *Physical Review Letters,* vol. 94, pp. 1-4 (2005).

[76] S. Rhodes, K. Nugent, and A. Roberts, "Precision measurement of the electromagnetic fields in the focal region of a high-numerical-aperture lens using a tapered fiber probe," *Journal of the Optical Society of America A,* vol. 19, pp. 1689-1693 (2002).

[77] Y. Fu, F. Ho, W. Lin, W. Liu, and D. Tsai, "Study of the focused laser spots generated by various polarized laser beam conditions," *Journal of Microscopy,*

vol. 210, pp. 225-228 (2003).

[78] A. Bouhelier, M. Beverslui, and L. Novotny, “Near-field scattering of longitudinal fields,” *Applied Physics Letters*, vol. 82, pp. 4596-4598 (2003).

[79] A. Nesci, R. Dandliker, and H. Herzig, “Quantitative amplitude and phase measurement by use of a heterodyne scanning near-field optical microscope,” *Optics Letters*, vol. 26, pp. 208-210 (2001).

[80] S. Bourzeix, J. Moison, F. Mignard, F. Barthe, A. Boccara, C. Licoppe, B. Mersali, M. Allovon, and A. Bruno, “Near-field optical imaging of light propagation in semiconductor waveguide structures,” *Applied Physics Letters*, vol. 73, pp. 1035-1037 (1998).

[81] J. Kim, D. Pride, J. Boyd, and H. Jackson, “Spectrally-resolved near-field investigation of proton implanted vertical cavity surface emitting lasers,” *Applied Physics Letters*, vol. 72, pp. 3112-3114 (1998).

[82] U. Ben-Ami, R. Nagar, N. Ben-Ami, J. Scheuer, M. Orenstein, G. Eisenstein, Lewis, E. Kapon, F. Reinhardt, P. Ils, and A. Gustafsson, “Near-field scanning optical microscopy studies of v-grooved quantum wire lasers,” *Applied Physics Letters*, vol. 73, pp.1619-1621 (1998).

[83] I. Sergey, S. Bozhevolnyi, B. Vohnsen, and E. Bozhevolnaya, “Transfer functions in collection scanning near-field optical microscopy,” *Optics Communications*, vol. 172, pp. 171-179 (1999).

[84] E. Hecht, “Optics,” 4th ed. *Addison-Wesley*, Reading, MA, pp. 469 (2002).

[85] B. Hecht, B. Sick, U. Wild, V. Deckert, R. Zenobi, O. Martin, and D. Pohl,

"Scanning near-field optical microscopy with aperture probes: fundamentals and applications," *Journal of Chemical Physics,* vol. 112, pp. 7761-7774 (2000).

[86] E. Rittweger, B. Rankin, V. Westphal, and S. Hell, "Fluorescence depletion mechanisms in super-resolving STED microscopy," *Chemical Physics Letters,* vol. 442, pp. 483-487 (2007).